

Exploring the Use of Multi-source High-Resolution Satellite Data for Snow Water Equivalent Reconstruction over Mountainous Catchments

Valentina Premier^{1,3}, Carlo Marin¹, Giacomo Bertoldi², Riccardo Barella¹, Claudia Notarnicola¹, and Lorenzo Bruzzone³

¹Institute for Earth Observation, Eurac Research, Viale Druso, 1 - 39100 Bolzano, Italy

²Institute for Alpine Environment, Eurac Research, Viale Druso, 1 - 39100 Bolzano, Italy

³Department of Information Engineering and Computer Science, University of Trento, Via Sommarive, 9 I - 38123 Povo, Italy

Correspondence: Valentina Premier (valentina.premier@eurac.edu)

Abstract. ~~Seasonal snow accumulation and release are so crucial for the hydrological cycle to the point that mountains have been claimed as~~ The hydrological cycle is strongly influenced by the accumulation and melting of seasonal snow. For this reason, mountains are often claimed to be the "water towers" of the world. ~~A key variable in this sense~~ In this context, a key variable is the snow water equivalent (SWE). However, the complex ~~accumulation and snow redistribution processes render~~ processes of snow accumulation, redistribution, and ablation make its quantification and prediction very challenging. In this work, we explore the use of multi-source data to reconstruct SWE at a high spatial resolution (HR) of 25 m ~~by proposing a novel approach designed for mountainous catchments~~. To this purpose, we ~~exploit i)~~ propose a novel approach based on i) in-situ snow precipitation data and Synthetic Aperture Radar (SAR) images to determine the pixel state, i.e. whether it is undergoing an SWE increase (accumulation) or decrease (ablation), ii) a daily HR time-series of snow cover area (SCA) maps derived by high- and low-resolution ~~optical-multispectral optical satellite~~ images to define the days of snow presence, ii and iii) a degree-day model driven by in-situ temperature to determine the potential melting, ~~and iii) in-situ snow depth and Synthetic Aperture Radar (SAR) images to determine the state of the catchment (i.e., accumulation or ablation) that is needed to add or remove SWE to the reconstruction~~. Given the typical high spatial heterogeneity of snow in mountainous areas, ~~HR data sample more adequately its distribution~~ the use of HR images represents an important novelty that allows us to sample its distribution more adequately, thus resulting in ~~a~~ a highly detailed spatialized information ~~that represents an important novelty~~. The proposed SWE reconstruction approach also foresees a novel SCA time-series regularization ~~from impossible transitions~~. ~~Moreover it reconstructs SWE for all the hydrological season without the need of~~ technique that models impossible transitions based on the pixel state, i.e. the erroneous change of the pixel class from snow to snow-free when it is expected to be in accumulation or equilibrium and, vice versa, from snow-free to snow when it is expected to be in ablation or equilibrium. Furthermore, it reconstructs the SWE for the entire hydrological season, including late snowfalls. The approach does not require spatialized precipitation information as input, ~~that which~~ that is usually affected by uncertainty. ~~Despite the simple approach based on a set of empirical assumptions, it shows good performances when tested~~ The method provided good results in two different test catchments: the South Fork ~~catchment~~ of the San Joaquin River, California, and the Schnals catchment, Italy, ~~showing a good~~

agreement with an average bias of -40 mm. It obtained good agreement both when evaluated against a HR spatialized reference product and of 38 mm when evaluated maps (showing an average bias of -22 mm) and against manual measurements (showing an average bias of -5 mm). The main sources of error introduced by each step of the method have been finally are discussed to provide insights about the applicability and future improvements into the main advantages and disadvantages of the method that may be of great interest for several hydrological and ecological applications.

1 Introduction

Seasonal snow accumulation and melting are of crucial importance melt are crucial for the hydrological cycle and the total water supply. Especially in mountainous areas, the snow has such a large impact on the local hydrology that mountains have been Mountains are claimed to be “the water towers of the world” (Immerzeel et al., 2020). For example, in the Alps the snowmelt contribution to the given the large impact of snow on local and global water resources (Immerzeel et al., 2020). The contribution of snow-dominated catchments to streamflow ranges from at least 50% of the 40% of total flow to some times over more than 95% (Viviroli et al., 2003). Hence, depending on the region (Viviroli et al., 2003). Therefore, it is essential to estimate the amount of water stored during the winter not only for river discharge forecasting but also for a correct planning of winter to forecast river discharge and to correctly plan human activities such as agriculture irrigation, drinking water supply, and hydropower production (Beniston et al., 2018; DeWalle and Rango, 2008). However, especially in (DeWalle and Rango, 2008; Beniston et al., 2018). In mountain regions, the snow distribution is highly variable in space and time due to redistribution processes (Balk and Elder, 2000) and precipitation observations are often affected by large errors due to orographic effects (Prein and Gobiet, 2017). This also limits the spatial accuracy of snow accumulation and melt models (Engel et al., 2017; Günther et al., 2019). In this context, given the difficulty to dispose of spatialized and continuous observations especially, thus limiting the effectiveness of available in-situ measurements. Especially in remote areas (Rees, 2005), continuous and spatialized observations are rare (Rees, 2005). Hence, remote sensing (RS) has shown to be represents a valuable tool for snow hydrology.

A correct spatial characterization of the snow properties requires both information knowledge about the extent of the snow cover, i.e., the snow cover area (SCA), and appropriate snowpack information. A key variable is the snow water equivalent (SWE), i.e., the total amount of water stored in the snowpack that would be released upon complete melting. While. Although a long list of methods for SCA detection SCA detection methods that exploit multispectral optical satellites is available in the literature (see Dietz et al. (2012) for a review) (e.g., Dietz et al., 2012; , 2018), we do not have operational methods to directly map SWE with high spatial resolution (HR). Direct SWE observations are limited to point measurements through by manual sampling, snow scales or snow pillows (Archer and Stewart, 1995; Meløysund et al., 2007), or with a limited spatial footprint (~ 500 m) as cosmic ray such as cosmic ray neutron probes (Schattan et al., 2019). Spatialized snow depth (SD) information can be provided by differential lidar altimetry (Painter et al., 2016) or stereo photogrammetry (Deschamps-Berger et al., 2020). Currently However, these methods can be applied only to limited areas and with a low temporal sampling. Moreover, to derive

the derivation of SWE from SD requires additional a priori information ~~is needed~~ to infer the snow density (Helfricht et al., 2018). Physically-based snow models represent a valid alternative (e.g., Lehning et al., 2006; Vionnet et al., 2012; Endrizzi et al., 2014) that can provide HR SWE information on large areas. ~~However~~Nonetheless, their accuracy is strongly limited by
60 the ~~availability of meteorological observations~~ uncertainty in the input data (Engel et al., 2017; Günther et al., 2019) and by the gravitational and wind-induced snow redistribution processes (Jost et al., 2007; Mott et al., 2018). One of the main challenges is to obtain an accurate precipitation field given the strong spatial variability of the variable related to orography, a generally scarce sampling density of the phenomenon that strongly influences the interpolation results, and possible inaccuracies in the measurements caused, for example, by undercatching (e.g., Prein and Gobiet, 2017).

65 ~~Active and passive~~ Passive and active microwave sensors can potentially provide information about the snowpack. In particular, ~~passive microwave sensors have been the first ones are~~ used to retrieve long time-series of SWE by exploiting the correlation between ~~the~~ brightness temperature and ~~the~~ SWE (Pulliainen et al., 2020). However, the observations are limited by a ~~poor spatial resolution (i.e., spatial resolution of 25 km) and mountain areas are excluded. The use of active microwave sensors and~~ are not suitable for mountain regions. Active microwave sensors, such as Synthetic Aperture Radars (~~SAR~~)has also been
70 investigated for the SARs), were investigated for HR retrieval of SWE (~~Shi et al., 1994; Baghdadi et al., 1997; Ulaby et al., 1981; Rott et al.~~ (Ulaby et al., 1981; Shi et al., 1994; Baghdadi et al., 1997; Rott et al., 2010) and differential SWE (Gunteriusen et al., 2001; Leinss et al., 2015). Despite the better spatial resolution~~also~~, active microwave sensors suffer ~~for from~~ the complexity of non-linear effects introduced on the total backscattering, such as snow layering, surface roughness, snow density, grain type and size, which in turn are all affected by the complex snow metamorphism and change in time. ~~Moreover, all~~ Furthermore, all
75 of these techniques work only in dry ~~conditions while snow conditions, whereas~~ the scarce penetration of the electromagnetic signal in wet conditions ~~is invalidating their applicability in monitoring the SWE evolution~~ invalidates their applicability to monitor the evolution of the SWE during the melting season. ~~Several review articles are available for more details about~~ For more details on SWE retrieval using SAR acquisitions, several review articles are available (e.g., Tsang et al., 2021).

80 ~~Even though~~ Despite recent developments, SAR is still far from providing unambiguous information on SWE ~~for all situations in all conditions. However,~~ it represents a promising tool to monitor the melting phases of the snowpack, i.e., the moistening, ripening, and runoff phases, or in other words, the presence and evolution of liquid water inside the snowpack ~~and its evolution (Marin et al., 2020). If (Marin et al., 2020). When~~ combined with optical data, the ~~runoff onset, onset of runoff~~ (i.e., the time when when the SWE reaches its maximum, does add) derived by SAR adds value to the ~~well-known concept of~~ the snow depletion curves snow depletion curve (SDC). SDC are functions that describe The SDC is a function that describes
85 the relationship between SCA and SD or SWE (Cline et al., 1998). Thus, time-series of SCA ~~maps~~ can be used to provide an indirect measurement of SWE (Yang et al., 2022). ~~Indeed,~~ SWE is a function of the duration of the snow cover, which intrinsically considers the energy exchanges responsible ~~of for~~ the melting process (Durand et al., 2008). For example, ~~a shallow snowpack~~ shallow snowpacks and high melt rates are associated with ~~a SDC with high derivative while a deep snowpack an SDC having a~~ high derivative, while deep snowpacks and low melt rates are characterized by a longer curve (e.g., Pimentel et al., 2015, 2017).
90 . Consequently, spatial accumulation and ~~melt variability~~ ablation variabilities, which are ~~linked to the geomorphology related~~

~~to the topography~~ of the study area (Anderton et al., 2002), result in different ~~snowpack persistence~~ persistence of the snowpack (Luce et al., 1998). Therefore, ~~by~~-knowing the SDC and the ~~maximum of SWE~~ SWE maximum at the end of the accumulation for ~~an area or an entire catchment~~, ~~it is possible to derive a catchment allows deriving~~ the evolution of SWE during ~~the~~-melt-
95 ing. This intuitive idea opens the possibility ~~to assimilate of assimilating~~ SCA and SDC ~~into physically based information into~~ physically-based snow models to correct ~~the~~-SWE evolution and improve ~~the~~-simulations (Arsenault and Houser, 2018).

~~In fact, another way to exploit the SDC for SWE estimation is the~~ Similarly, SDC can be exploited in combination with distributed snowmelt models to reconstruct SWE time-series in ~~re-analysis (Martinec and Rango, 1981; ?; Rittger et al., 2016)~~ re-analysis (Martinec and Rango, 1981; Molotch and Margulis, 2008; Rittger et al., 2016). ~~Differently from reanalysis (Martinec and Rango, 1981; Molotch and Margulis, 2008; Rittger et al., 2016)~~. Unlike the meth-
100 ods that require ~~to know the precipitations and the meteorological forces that~~ known precipitations and meteorological forces ~~to~~ redistribute the snowpack during the accumulation, SWE reconstruction builds the SWE ~~timeseries~~ time-series backward from the last day of snow presence up to the peak of accumulation ~~by exploiting~~. ~~To this purpose, these approaches exploit~~ the estimation of the potential melt energy and the knowledge about the presence of snow cover, ~~simplifying in this way thus~~ simplifying the solution of the problem. SWE reconstruction approaches show good ~~performances over large basin performance~~ performances over large basins
105 over large basins and even mountain ranges, outperforming the accuracy provided by snow models or spatial interpolation approaches of in-situ SWE measurements (Bair et al., 2016). Nevertheless, the accuracy of the results depends on a robust estimation of both the ~~SCA and the melt energy. For this purpose~~ potential melting and SCA. For the first one, several methods ~~have been proposed for the computation of the potential melt energy were proposed~~ that range from a simple yet robust ~~degree day~~ degree-day (DD) model (Martinec and Rango, 1981) to a complete radiation energy computation that also takes
110 into account ~~also~~ the snow albedo (Bair et al., 2016). ~~These models generally consider a calibration factor that balances out the possible inaccuracies providing accurate results. Furthermore, the derivation of the HR SCA is hampered by the cloud presence (e.g., Premier et al., 2021). In this regards the~~ To estimate SCA, many works presented in the literature ~~exploited only exploit~~ low-resolution (LR) ~~images since the~~ multispectral satellite images, since their large swath allows a high repetition time, i.e., with a daily or sub-daily ~~acquisitions, mitigating in this way cloud obstruction acquisition. This mitigates~~ cloud obstruction issues and involves a proper SCA sampling. However, ~~the LR images are not providing the spatial details, in the Shannon sense, that allow a proper sampling~~ LR images do not provide sufficient spatial detail on the variability of the snow cover evolution in the mountains, which is ~~in on~~ the order of ~~few dozen of a few dozen~~ meters. Moreover, the use of LR ~~sensors images~~ results in a non-linear combination of the different contributions of the elements within the pixel ~~and this should be properly taken into account by~~, ~~and this may induce large errors in~~ the snow classification approach ~~to avoid large~~ errors,
120 especially in complex terrains. On the other hand, the use of HR snow maps introduces important benefits ~~both in SWE determination as well as in streamflow forecasting (Li et al., 2019)~~ in both determining SWE and forecasting streamflow (Molotch and Margulis, 2008; Li et al., 2019). Landsat products were used to retrieve SCA in many papers in the literature (e.g., Molotch et al., 2004; Molotch and Bales, 2005, 2006). However, a Landsat satellite acquires an image every 16 days (at the equator). With the introduction of the Copernicus Sentinel-2 (S2) mission, ~~the~~-HR images are made available ~~free of charge~~ with a temporal resolution at the equator ~~with an improved temporal resolution~~ of 5 days (at the equator). This opens up new opportunities to monitor ~~the~~-heterogeneous snow conditions in the mountains. ~~However~~ Unfortunately, due to ~~the~~-cloud cover-

age, ~~the~~ useful acquisitions are reduced by 50% in the Alps (Parajka and Blöschl, 2006). ~~Thus~~Therefore, even if the Landsat images are exploited together with the S2 images, only a few acquisitions are available per month. Recently, we proposed an approach to the reconstruction of daily HR snow cover maps. The approach performs a gap-filling and a downscaling of the snow cover fraction (SCF) maps derived at LR based on the idea that the melting and accumulation patterns ~~are repeating~~ inter-annually repeat interannually (Premier et al., 2021; Revuelto et al., 2021). Therefore, by observing partial HR or LR acquisitions it is possible to reconstruct a daily HR snow cover.

~~In this paper we explore~~ This work explores the use of multi-source satellite data to reconstruct HR SWE for a given catchment. ~~The approach exploits:~~ The approach exploits: i) daily HR snow cover daily SWE time-series ~~derived by fusion of high- and low-resolution optical sensors to determine the dates of snow appearance and disappearance,~~ ii) potential melting ~~derived by in-situ temperature observations with a degree-day (DD) model,~~ iii) in-situ SD/SWE observations to determine the *accumulation* state, and iv) SAR information to determine the *ablation* state. ~~In detail, the method starts with the determination of the catchment state, i.e. at a spatial resolution of 25 m. To achieve such detail, we propose as main novelties the use of a daily HR SCA time-series together with accurate information on the melting phase from SAR data. To this purpose, we also introduce the concept of the snow state of a pixel, which represents the direction of the change in SWE for that pixel, that is, accumulation (SWE increase) or, ablation (SWE decrease) or equilibrium (constant SWE). This allows reconstructing SWE without the need for spatialized precipitation data. Indeed, the method redistributes the amount of melting by exploiting the information about the state rather than quantifying the precipitation input. According to the state, that is assumed to be homogeneous for all the pixels of the catchment, we regularize the HR SCA time-series from impossible transitions to correctly estimate the dates of snow appearance and disappearance for each pixel. This simplificative assumption is a consequence of technological limitations in spatializing this information. The state information is needed together with the potential melting to reconstruct the daily HR SWE maps with a resolution of 25 m by adding or removing SWE according to the catchment state. Note that the reconstruction also includes the accumulation phase without the need of precipitation data as input, which are often unreliable over complex terrains. The main novelties of the proposed approach are: i) the generation of daily HR SWE maps, ii) the~~ Moreover, the state allows us to set up a novel regularization of the ~~daily HR SCA time-series from impossible transitions,~~ and iii) ~~the precipitation independent SWE reconstruction. The approach has been validated in two~~. In the paper, we also present a critical analysis of the main sources of error to provide insights into the main advantages and disadvantages of the method that may be of great interest for several hydrological and ecological applications. We explore the applicability of the method to two mountainous catchments: i) the South Fork ~~catchment of the San Joaquin River (SFSJR)~~, located in the Sierra Nevada - California (USA), and ii) the Schnals catchment, located in the Alps - South Tyrol ~~, Italy~~ (Italy).

The paper is structured into five sections. Sec. 2 presents the different steps of the proposed approach to reconstruct the daily HR SWE. The two test sites ~~and the used~~ considered for experimental validation and the related dataset are presented in Sec. 3. ~~The obtained results~~ results obtained are illustrated in Sec. 4. ~~A detailed discussion on the approach advantages and limitations~~

~~and on the results follows in~~ In Sec. 5, we discuss the main sources of errors of the method and the novel SCA regularization. Finally, Sec. 6 draws the conclusions of the work and gives indications for further exploitation of the proposed approach.

2 Proposed approach to HR SWE reconstruction

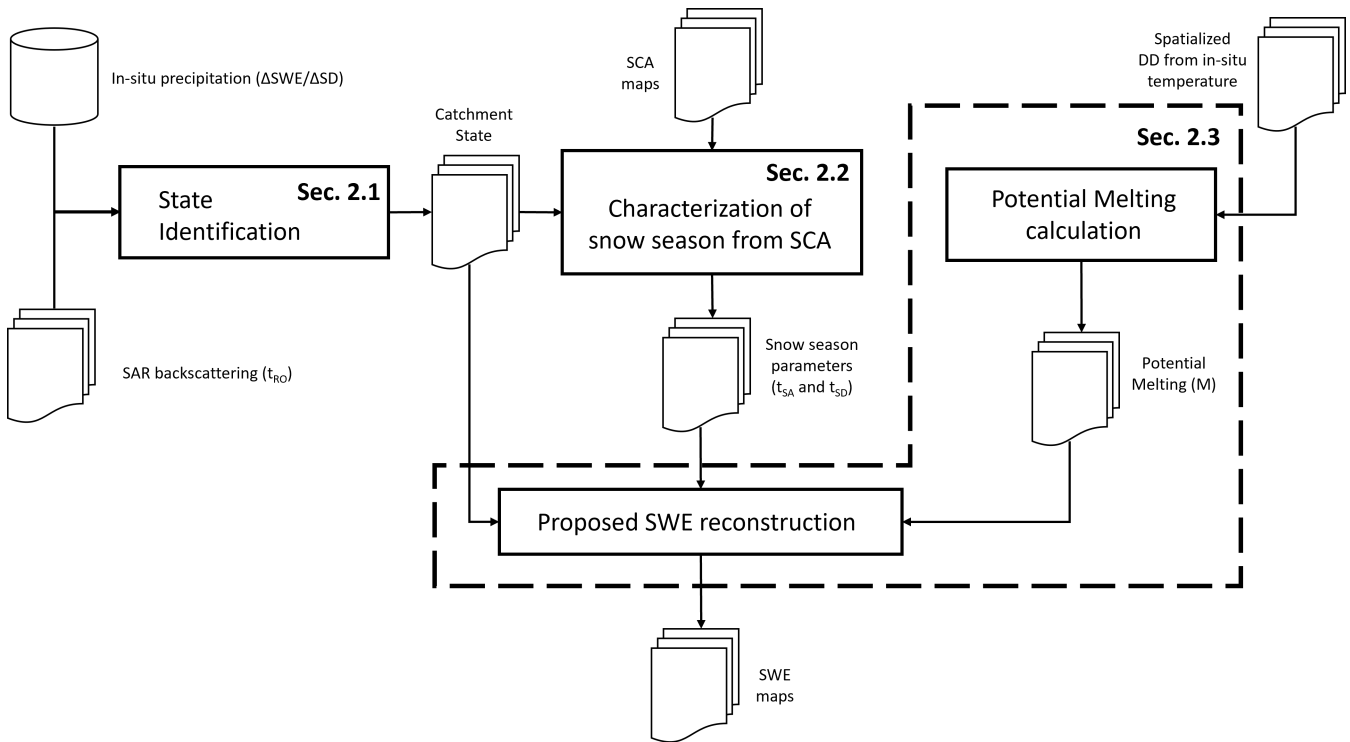
~~In this section, the proposed approach to HR SWE reconstruction will be presented. The~~ The presented approach is made up of three main parts: i) ~~the~~ identification of the ~~catchment~~ state, ii) ~~the~~ characterization of the snow season from the regularized SCA time-series, and iii) ~~the SWE calculation~~ calculation of the SWE. The details will be illustrated in the ~~three next following three~~ subsections. As depicted in Fig. 1, the method ~~initially determines the state of the catchment~~ starts with the identification of the state, i.e., accumulation, ablation or equilibrium (see Sec. 2.1). ~~This allows to properly reconstruct SWE in case of solid precipitations after the peak of accumulation and also to redistribute the total amount of SWE calculated for the melting in the accumulation period. Both cases are generally omitted in state-of-the-art SWE reconstruction methods (e.g., Martinec and Rango, 1981). Moreover, the catchment~~ The state information is used both to regularize the SCA time-series ~~of SCA from taking into account~~ impossible transitions and to correctly determine the beginning and end of the season (see Sec. 2.2). ~~Finally, from the potential melting and the~~ With impossible transitions, we indicate an erroneous change of the pixel class from snow to snow-free when the state is accumulation or equilibrium, or vice versa, the change from snow-free to snow when the state is ablation or equilibrium. The regularized time-series of SCA ~~the proposed approach reconstructs~~ is then used with the potential melting to reconstruct the daily HR SWE maps (see Sec. 2.3). The state information is used again in this step i) to redistribute the total amount of SWE calculated for the melting in the accumulation period, and ii) to include late snowfalls that occur after the peak of accumulation to the reconstruction. Both cases are generally omitted in state-of-the-art SWE reconstruction methods (e.g., Martinec and Rango, 1981; Molotch and Margulis, 2008).

2.1 Identification of the catchment state

~~The proposed reconstruction approach is designed for a hydrological catchment that is subjected to similar weather forcings and consequently to similar accumulation and ablation events i. e., the catchment is not too vast. If we take this assumption strictly, we can define three states that describe the three~~

2.1 Identification of the state

~~Let us introduce the three states that describe~~ possible SWE changes within a pixel, i.e., ΔSWE between two times $t - 1$ and t . ~~These states are~~ As illustrated in Table 1, the states are: i) accumulation which represents an increase in SWE ($\Delta\text{SWE} > 0$), ii) ablation which represents a reduction in SWE ($\Delta\text{SWE} < 0$) ~~and~~, and iii) equilibrium which represents a stable SWE ($\Delta\text{SWE} = 0$), as shown in Fig. ~~??~~. The identification of the state is necessary in the proposed approach to decide whether SWE is added or removed for the reconstruction (see Sec. 2.3). In detail, the catchment state does not only characterize the change in terms of SWE but also in terms of SCA, if observable, as described as follows: *Accumulation* when the total $\Delta\text{SWE} > 0$ due



Workflow of the proposed approach showing the three main steps: i) state identification, ii) characterization of snow season from SCA, and iii) SWE reconstruction. The inputs are: i) a HR-SCA time-series and daily spatialized DD maps derived from AWS, ii) SAR backscattering time-series, and iii) SWE or SD from automatic weather stations (AWS). As output, we obtain the daily HR SWE maps.


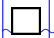
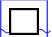









Figure 1. Workflow of the proposed approach showing the three main steps: i) state identification, ii) characterization of snow season from SCA, and iii) SWE reconstruction. The inputs are: i) SWE or SD from automatic weather stations (AWSs), ii) SAR backscattering time-series, iii) a daily HR SCA time-series, and iv) daily spatialized potential melting maps derived from AWSs. As output, we obtain the daily HR SWE maps.



to a snowfall. We can either observe i) a positive ΔSCA , if the snow covers the bare ground, or ii) $\Delta SCA = 0$, if the snowfall happens at higher elevation than the actual snowline.

The phenomena that cause an SWE variation are several, such as snowfall, melting, sublimation, human activities, or redistribution due to wind or gravitational transport, e.g., avalanches. However, ΔSCA is never negative and consequently a single pixel can not turn from snow to snow-free accumulation from $t-1$ to t . So, depending on the extension of the snowfall, and to melting if ablation. Indeed, we propose to estimate the SWE to be added to the reconstruction by considering a quantity proportional to the spatial SWE increment can interest the total snow-covered area or a part of the catchment. It is usually a rapid event – one to a couple of days (Thorp and Scott, 1982).

Ablation when the total $\Delta SWE < 0$ due to any kind of energy exchanges (as increasing temperature, solar radiation, or rain-on-snow). We can either observe a negative ΔSCA , if the snowpack is completely melted out and shows the bare ground,

Table 1. Definition of the three possible states: *accumulation*, *ablation* and *equilibrium*. The possible class transitions at pixel level associated with the state are described.

State	ΔSWE	Class transition		Description
		t-1	t	
Accumulation	>0			<u>Snow on bare ground</u>
				<u>Snow on snow</u>
Ablation	<0			<u>Snowpack disappearance</u>
				<u>Snowpack reduction</u>
Equilibrium	=0			<u>Stable snowpack</u>
				<u>Bare ground</u>

Legend:  = snow  = snow-free

or $\Delta SCA = 0$, if the melting is only affecting the height of the snowpack. However, ΔSCA is never positive and a pixel can not turn from *snow-free* to *snow* from $t-1$ to t . So, depending on snow depth/SWE variations. Thus, in an ideal case, we include only fresh snow as the main driver. Similarly, the amount of energy and on the depth of the snowpack, the spatial SWE decrement can interest the total SCA or a part of the catchment. It can be a long period, especially in the last phase of the season.

Equilibrium SWE to be subtracted is calculated using a DD model and, therefore, it only represents melted snow. Trivially, SWE remains constant when $\Delta SWE = 0$. This is the case of a steady state, i.e., no changes within the catchment, or redistribution due to wind or gravitational transport, e.g. *equilibrium*. Note that the state is defined on a daily scale, avalanches. This last condition does not affect the overall SWE balance that remains constant, even though we can have local deposition and erosion looking at a pixel scale. In terms of ΔSCA , these changes are mainly increments of *snow-free* pixels, hence a pixel can not turn from *snow-free* to *snow* from $t-1$ to t . In fact, we expect that snow moves from exposed areas – that can become *snow-free* – to sheltered areas – that were already covered by snow, due to the terrain properties that facilitate snow deposition.

Definition of the three possible catchment states: *accumulation*, *ablation* and *equilibrium*. The description of the possible events that characterize the catchment between two consecutive dates is reported together with the difference in terms of SWE and SCA. As one can notice only ΔSWE can be used to unambiguously identify the three states. The illustrations represent the SCA in an idealized catchment where white and brown areas are the *snow* and *snow-free* areas, respectively and the dashed lines represent the contour lines, which corresponds to the temporal resolution of the exploited HR SCA time-series. In this work, the diurnal fluctuations in meteorological forces are not considered.

To determine the catchment state according to the aforementioned definitions The state varies pixel-wise due to the topography and meteorology of the study area. However, it is clear that ΔSCA is ambiguous and consequently we need to estimate if SWE is increasing, decreasing or is constant. This information difficult to extrapolate this information with the necessary spatial

detail. In the following paragraphs, we propose simplified strategies for the *accumulation* and *ablation* determination. If none of them is identified, the state is *equilibrium*.

2.1.1 Accumulation identification

The accumulation identification can be retrieved ~~by from~~ a network of automatic weather ~~station~~ stations (AWSs) that provide continuous information about the occurrence and elevation of snowfall events, ~~e.g. for example,~~ direct SWE measurements or indirect precipitation/SD measurements. ~~While Although~~ continuous SWE measurements are ~~hardly available, by mean of~~ scarcely available, using pluviometers and temperature observations, it is possible to split precipitation between liquid and solid (Mair et al., 2013) and identify the ~~catchment state accordingly, but with the limitation that they state accordingly.~~ However, these stations are rarely installed at high elevations. SD sensors are more suitable for our purpose, but their observations are often affected by wind and gravitational transport, leading to deposition/removal that ~~may can~~ be falsely interpreted as *accumulation/ablation*. Hence, even if the ~~AWS AWSs~~ are generally situated in locations undisturbed from the wind action, it is more convenient to dispose of a large number of ~~AWS AWSs~~ that need to be ~~screened filtered~~ to exclude possible sensor errors or wind/gravitational redistribution. For these reasons, the increase in SWE/SD ~~increment~~ should be greater than a certain threshold SD_{min}/SWE_{min} that is fixed at 2 cm for SD according to the values found in the literature (Engel et al., 2017), resulting in a value of 2 mm for SWE when considering the typical density of fresh snow (100 kg/m³).

~~Nevertheless, the general scarce availability of distributed measurements inside a given catchment render the localization of the accumulation and ablation events very challenging and therefore the definition~~ It is important to note that a station is representative of a limited area whose extension is highly variable depending on the complexity of the terrain. In the case of a well-monitored area with stations distributed with elevation, it is possible to divide the catchment into different elevation belts where the snowfall events can be considered nearly homogeneous. However, in many basins, this might be far from reality. As a common configuration for snow monitoring, we have a single station located at a high point of the catchment, which is informative enough to identify the accumulation events but not their extent. Furthermore, it has been shown in the literature that estimating the snowfall limit can be very challenging (e.g., Fehlmann et al., 2018). In a poorly monitored catchment, we consider that snowfalls occur throughout the snow-covered area of the catchment ~~state prone to error.~~ We acknowledge that this assumption may result in less accurate SWE estimation, especially in the case of mixed states. For example, snowfall can be observed at high elevations, together with rain-on-snow at low elevations, causing snowmelt. However, we assume that the effect of these events on the total SWE balance is small enough to be considered negligible as we will discuss in Sec. 5.2.

250

In summary, when the AWSs show an increment greater than a defined threshold, we identify the state as *accumulation*.

2.1.2 Ablation identification

The ablation can be identified by using a snowmelt model. We consider here the simple temperature index model, which is an empirical model that takes advantage of the intuitive concept that air temperature is a proxy of melting. When the temperature exceeds a fixed threshold, we expect that the pixel melts. However, this is a simplified approach that does not consider all

255

the components that contribute to snowmelt. More complex formulations include estimates of radiation, sensible heat, latent heat, and ground heat fluxes (e.g., Ismail et al., 2023). Moreover, temperature observations may be sparse, thus affecting the accuracy of the spatialization.

260 Multi-temporal SAR observations have shown to be of great potentiality and to be able to SAR observations derived from Sentinel-1 (S1) can detect the presence of a melted snowpack melting snowpack, as explained by Marin et al. (2020). In this work The authors investigated the relationship between the SAR backscattering and the three melting phases have been investigated. It has been shown that when the backscattering is interested by, i.e., the moistening, ripening, and runoff phase. In detail, they showed that if the SAR backscattering presents a decrease of at least 2 dB, the snowpack is assumed to get moistened (Nagler and Rott, 2000). The minimum of the backscattering corresponds instead with the maximum of SWE. After that moment, the snowpack starts to release water and enters in the so-called gets moistened (Nagler and Rott, 2000). Initially, at the beginning of the moistening phase this decrease affects only the afternoon measurements. When it also affects the morning measures, the ripening phase starts. Finally, the backscattering increases as soon as the SWE starts to decrease, which corresponds to the beginning of the runoff phase. This moment represents the most important contribution to first contribution of the snowpack to the release of water. Empirical experiments on five selected test sites showed that the melting phases were 270 identified with an RMSE of 6 days for the water release and can be provided in a HR spazialized manner, i.e., marking the dates of ablation for each pixel. moistening phase, 4 days for the ripening phase, and 7 days for the runoff phase.

On the other hand, at the best of our knowledge there are no remotely sensed data that can be exploited The multi-temporal analysis of the SAR backscattering represents a novel way to identify the snowfalls ongoing melting in a spatialized HR manner and that can be used to identify the accumulation at the level of each single pixel. In manner. The runoff onset (t_{RO}) 275 represents the time when the snowpack is isothermal. In this way, information about the cold content of the snowpack is incorporated into the DD model excluding incorrect early melting. However, the methodology presented by Marin et al. (2020) may fail in areas such as forests. For this reason, we propose applying the method only if a pixel presents the characteristic "U-shape" signature of the backscattering signal. To this purpose, we apply a multi-temporal analysis to the majority of the situations, only one AWS located at a given high point of the catchment (which is a common configuration for snow monitoring) 280 would be informative enough to identify all the accumulation events, but this may introduce errors in particular cases of mixed conditions. For example, it is possible to observe snowfalls at high elevations, rain on snow at low quotes that cause snowmelt and even steady state conditions for mid-altitude belts. A correct characterization of such a situation requires to consider different areas with different states separately, which for the moment is out of the scope of the paper. We will discuss the limitations and possible future steps to improve this aspect in Sec. ?? different available S-1 tracks. First, we identify if a drop 285 of at least -2B is present in the time-series. Second, the minimum is selected after this drop. When more tracks are available, we set the first minimum as the beginning of the runoff. Therefore, we propose to consider in ablation a pixel for the entire period ranging from the backscattering minimum to the disappearance of the snow cover identified by optical-derived time series. For the pixels that do not present the characteristic "U-shape", we rely on the DD model for the identification of the melting state.

In summary we propose a hybrid approach to identify the state by satisfying the following necessary conditions in order 290 of priority, we propose identifying the state of ablation for a specific date and a single pixel if the following conditions are

met: i) there is no accumulation when the AWS show an increment greater than a defined threshold on the date in question,
ii) ablation when the SAR backscattering presents shows an increase after a relevant drop (and not accumulation), and iii)
equilibrium otherwise. In this way, even though the accumulation does not allow to correctly spatialize the snowfalls, a
spatialized information on the ablation allows to distinguish among pixels that are really subjected to melting and pixels
295 that do not experience any change. In other words, a coexistent ablation and equilibrium is possible. Finally, it is worth to
mention that mixed situations within the same day and for the same area are also possible given diurnal fluctuations in the
meteorological forces. However in this work, we do not consider sub-daily variations but only changes that are sampled in the
temporal resolution of the exploited HR SCA time-series, i.e., one day, of at least -2dB, indicating that the minimum value
corresponding to t_{RO} has been reached, and iii) the degree day (as shown in Eq. 2) is greater than 0.

300 2.2 Characterization of the snow season from regularized SCA time-series

A HR SCA is an input needed necessary input for the proposed SWE retrieval , as it is used to estimate is a daily HR
SCA time-series, or in other words, the date of snow appearance t_{SA} and disappearance t_{SD} . As mentioned in the Intro-
duction, such a product is not available directly from remotely sensed images due to limitations in the revisit time and cloud
contamination obstruction. Therefore, there is the need to reconstruct a daily HR SCA it is necessary to reconstruct it. Among
305 the several various methods present in the literature, we used use the approach proposed by Premier et al. (2021), which merges
the information coming from a sparse long HR time-series and a continuous daily LR time-series acquired in the period of in-
terest. Gap-filling and downscaling steps are performed by applying a set of hierarchical rules based on historical analyses and
geomorphometrical analyzes and topographical features. The main idea behind the approach is that snow patterns are persistent
persist over time and follow a regular distribution that is strongly dependent on the geomorphology topography and meteorol-
310 ogy of the area of interest (Mendoza et al., 2020). We refer the reader to Premier et al. (2021) for the details.

Despite the generally accurate results of the above-mentioned approach , the output HR SCA (the overall accuracy is
empirically estimated to be around 92%), the HR SCA output is still affected by possible inconsistencies. Errors may arise
either from the classification algorithm applied to the multi-spectral multispectral input images or from the reconstruction ap-
315 proach. By applying the approach presented in Premier et al. (2021) In detail, we can highlight the presence of two main sources
of errors: i) an underestimation of snow presence in forested areas when the snow falls below the canopy and thus is not visible
anymore from the satellite point of view , (i.e., snow on ground the ground), and ii) the missed identification of snow-patches
at the end of the season. The first error source is due to the fact that the classification methods used for snow retrieval for both
HR and LR data relay images rely only on the spectral information measured inside the resolution cell of the sensor without
320 a dedicated module for inferring the presence of snow if when hidden by the canopy. This affects the detection of snow on
ground the ground, particularly for HR images, since the small resolution cell is likely to contain a majority fraction of canopy
the canopy, especially over very dense forests. This problem is instead mitigated for LR pixels that are likely to contain not
only forested areas but also open fields where the snow is visible, increasing in this way the possibility to detect of detecting the
snow presence. Hence, in the daily time-series of SCA, a discontinuity that happens mainly when HR images are acquired, can

325 ~~be identified as a local decrease of SCA~~Therefore, it is possible to observe local decreases in SCA mainly in correspondence
with an HR acquisition. The second error involves mostly LR images whose spatial detail is not enough to detect mixed pixels
with low SCF. ~~It~~This is an error that persists over time since LR acquisitions are more frequent than HR acquisitions. ~~In other~~
~~words, in both cases snow-free pixels may be falsely detected, i.e., false negative (FN) errors. Snow pixels can also be falsely~~
~~detected i.e., a false positive (FP) errors due mainly to possible residual misclassified clouds that are identified as snow – this~~
330 ~~is usually an error isolated in time. All these errors are detectable by looking at the class transitions in the time-series of each~~
~~pixel: the snow presence is not smooth in time. This results in an erroneous SWE determination that is strongly related to the~~
~~persistence of the snow, requiring a regularized time-series.~~, while a local increase of SCA is shown in correspondence with
an HR acquisition.

~~A helpful information~~The state concept introduced in Sec. 2.1 can be used to regularize the SCA~~is the state of the catchment~~
335 ~~that is daily identified by following the rules described in the previous subsection. If the snow cover maps. According to Table~~
~~1, only transitions of the pixel class that~~ are coherent with the state ~~– it follows that: i) if~~ are allowed. When *accumulation*
~~– all the pixels the pixel~~ can only turn from *snow-free* to *snow* or ~~maintain their label, and ii) if~~ *ablation* or ~~if snow falls on~~
~~bare ground, or it can continue to be~~ *equilibrium*, ~~all the pixels snow~~ if snow falls on already deposited snow. Similarly, when
ablation the pixel can only turn from *snow* to *snow-free* or ~~maintain their label. Since~~ *ablation* ~~and if the snow cover disappears,~~
340 ~~or it can remain snow if the snow cover partially melts. Finally, when~~ *equilibrium* ~~imply the same rule as explained also in Sec.~~
~~2.1, we will refer more generally to the pixel continues to be snow or snow-free depending on the situation. Therefore, we can~~
~~define the impossible transitions: i) a pixel cannot turn from snow to~~ *ablation* ~~snow-free only. In other words, t_{SA} and t_{SD} may~~
~~vary for each pixel but for sake of coherence they must coincide with an~~ ~~from $t - 1$ to t if~~ *accumulation* or *equilibrium*, and ii)
345 ~~a pixel cannot turn from~~ *accumulation* ~~and an snow-free to snow from $t - 1$ to t if~~ *ablation* ~~date, respectively. Pixels that do not~~
~~respect these rules are potential mistakes that need to be corrected. When we face with an erroneous class or~~ *equilibrium*.

When facing a *wrong* transition, we do not know a priori ~~if whether~~ the correct label is the one at $t - 1$ or the one at t . To
~~understand what is the correct solution~~derive the correct interpretation, we consider an appropriate time window and compute
the most frequent label ~~for it according to a~~ ~~according to the~~ majority rule. The time window is chosen ~~in a different way~~
~~differently~~ in the case ~~that where~~ we are facing ~~with~~ a recent or an old date of snow appearance t_{SA} . In detail, for a given pixel,
350 we consider:

- a *recent date of snow appearance* when $t - t_{SA} < 10$ days. ~~We observe in this period~~FN mostly due to ~~In this period, we~~
~~often observe~~ missed detection of snow under ~~canopy the canopy~~, especially by HR sensors. ~~In~~Under this condition, we
do not expect fast changes ~~since temperatures are low~~, ~~since the temperatures are likely to be low~~, and thus the potential
melting is low (see Eq. 1). ~~Accordingly~~Consequently, we propose to consider a daily time window of ± 5 days from t to
355 check what is the most persistent label of the considered pixel (Parajka and Blöschl, 2006);
- an *old date of snow appearance* when $t - t_{SA} > 10$ days. If the final melting has already started, changes may be quick,
and the most common situation is the missed detection of mixed pixels as snow patches. We observe that in this period
HR sensors detect snow patches that are completely omitted by LR sensors. In this case: i) the dates after t are not

360 informative since the snow patches ~~are disappearing~~ disappear quickly, and ii) daily SCA may not be informative when ~~it is derived by~~ derived from LR. For this reason, we consider only the last ~~up to 5 dates when a~~ up to five dates when ~~an~~ HR was originally acquired in a time window between t_{SA} and t .

Once we ~~have determined~~ determine the state and whether ~~if~~ we are handling ~~with~~ a recent or ~~an~~ old t_{SA} , we can compute the most frequent label in the considered time window and apply the following correction (see Algorithm 1).

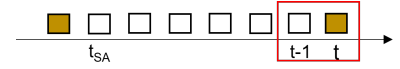
365 The correction is performed by advancing forward in time, i.e., we assume that ~~the~~ the previous labels are always coherent with ~~the~~ the previous states. ~~The correction itself cannot introduce inconsistencies. In case~~ If we are in *accumulation* or *equilibrium*, a transition from *snow* to *snow-free* is not allowed. If the pixel is ~~labelled as~~ labeled *snow* ~~at in~~ at in $t - 1$, ~~then~~ it means that ~~for~~ for the sake of coherence ~~it turned to~~ it turned into *snow* ~~at in~~ at in t_{SA} . We also know the date of the ~~last ablation after~~ last ~~t_{SA} most recent ablation~~ most recent ablation t_{lastAB} , i.e., ~~t_{lastAB} with~~ t_{lastAB} with $t_{SA} \leq t_{lastAB} \leq t - 1$. ~~Hence~~ the last chance that the pixel had to become *snow-free*. ~~Therefore~~, we compute the most frequent label accordingly with the majority ~~rules~~ rule described in the previous
370 paragraph ~~which vary depending if~~ which varies depending on whether the snowfall is old or recent. If ~~it results that~~ i) t is a false negative (FN), we can simply set it as i) the most frequent label is *snow*, t is replaced with *snow*; ii) ~~$t - 1$ is a false positive (FP), we need to replace~~ the most frequent label is *snow-free*, all times starting from the day of the last ablation state t_{lastAB} (or t_{SA} , ~~in case the last ablation precedes~~ in case the last ablation precedes t_{SA}) ~~until~~ until $t_{lastAB} < t_{SA}$ ~~up to~~ up to $t - 1$ ~~are replaced~~ are replaced with *snow-free*, ~~since the transition *snow* to *snow-free* can happen during ablation only.~~

375 Analogously, the transition from *snow-free* to *snow* is not allowed in *ablation* or *equilibrium*. If the pixel is ~~labelled~~ labeled as *snow-free* at $t - 1$, it means that ~~for~~ for the sake of coherence, ~~it turned to~~ it turned to *snow-free* at t_{SD} . We also know the date of the ~~last accumulation after~~ last ~~t_{SD} most recent accumulation~~ most recent accumulation t_{lastAC} , i.e., ~~t_{lastAC} with~~ t_{lastAC} with $t_{SD} \leq t_{lastAC} \leq t - 1$ ~~the last chance that the pixel had to become~~ the last chance that the pixel had to become *snow*. Hence, we compute the most frequent label accordingly with the majority ~~rules~~ rule, and if it results that
380 i) ~~t is a false positive (FP), we simply set it as~~ the most frequent label is *snow-free*, t is replaced with *snow-free*; ii) ~~$t - 1$ is a false negative (FN), we need to replace~~ the most frequent label is *snow*, all times starting from the day of the last accumulation state t_{lastAC} (or t_{SD} , ~~in case the last accumulation precedes~~ in case the last accumulation precedes t_{SD}) ~~until~~ until $t_{lastAC} < t_{SD}$ ~~up to~~ up to $t - 1$ ~~with *snow-free* since the transition *snow-free* to *snow* can happen during ablation only.~~

Algorithm 1 Regularization of the snow cover maps with the **catchment**-state.

if *Accumulation or Equilibrium* then

Transition *snow to snow-free* is not allowed!



The pixel is *snow* from $t_{SA} \leq t - 1$. Between t_{SA} and $t - 1$ all states are possible.

We indicate with t_{lastAB} a day $t_{SA} \leq t_{lastAB} \leq t - 1$ representing the date of the last ablation after t_{SA}

$t_{lastAB} :=$ most recent ablation date, i.e. last chance to get *snow-free*. If $t_{lastAB} < t_{SA}$ then $t_{lastAB} = t_{SA}$

if $t - t_{SA} < 10$ days then

| **Recent** t_{SA} : check $t \pm 5$ days and compute the most frequent label

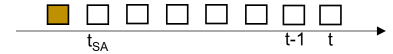
else

| **Old** t_{SA} : check last up to 5 HR from t_{SA} to t and compute the most frequent label

end

if most frequent label is *snow* then

| t is a FN (e.g., missed snow under canopy): set t as *snow*



else

| $t - 1$ is a FP (e.g., cloud detected as snow): set $[t_{lastAB}; t - 1]$ as *snow-free*



end

if *Ablation or Equilibrium* then

Transition *snow-free to snow* is not allowed!



The pixel is *snow-free* from $t_{SD} \leq t - 1$. Between t_{SD} and $t - 1$ all states are possible.

We indicate with t_{lastAC} a day $t_{SD} \leq t_{lastAC} \leq t - 1$ representing the date of the last accumulation after t_{SD}

$t_{lastAC} :=$ most recent accumulation date, i.e. last chance to get *snow*. If $t_{lastAC} < t_{SD}$ then $t_{lastAC} = t_{SD}$

if $t - t_{SA} < 10$ days then

| **Recent** t_{SA} : check $t \pm 5$ days and compute the most frequent label

else

| **Old** t_{SA} : check last up to 5 HR from t_{SA} to t and compute the most frequent label

end

if most frequent label is *snow* then

| $t - 1$ is a FN (e.g., missed snow patches): set $[t_{lastAC}; t - 1]$ as *snow*



else

| t is a FP (e.g., cloud detected as snow): set $t - 1$ as *snow-free*



end

2.3 HR SWE reconstruction

Once the catchment state has been defined for each day ~~Once the state is defined~~ as described in [Sec. 2.1](#), and the daily HR SCA
 385 time-series ~~has been regularized with the catchment is regularized coherently with the~~ state as described in [section 2.2, Sec. 2.2](#), we can apply the proposed approach to ~~the~~ HR SWE reconstruction ~~can be initiated. This operation requires to calculate.~~
~~As illustrated in Fig. 2, this operation requires calculating~~ the total amount of melting and ~~redistribute~~ ~~redistributing~~ it during
 the snow season according to the preservation of ~~the~~ mass and the ~~catchment state. For this purpose~~ ~~state. To this purpose~~, we
 estimate the daily potential melting with the ~~degree day (DD)~~ ~~DD~~ model. For a generic time interval $[t-1; t]$, the potential
 390 melting $M_{t-1,t}$ is estimated through the following equation:

$$M_{t-1,t} [mm] = a [mm^{\circ}C^{-1}d^{-1}] \cdot DD_{t-1,t} [^{\circ}Cd] \text{ if } t > t_{RO} \quad (1)$$

where a is the ~~so-called so-called~~ DD factor and varies depending on the ~~considered area as well on the considered area~~
~~and the~~ snow period. ~~Note that potential melting is considered only after the runoff onset as detected by S1 data.~~ We used a
 value of $a = 4.5 \text{ mm}^{\circ}C^{-1}d^{-1}$ for the ~~South Fork catchment SFSJR~~ and $a = 5.2 \text{ mm}^{\circ}C^{-1}d^{-1}$ for the Schnals catchment.
 395 The coefficient is calibrated by considering ~~the~~ measured SWE and temperature at the AWSs (if available) and ~~also~~ taking
 into account ~~also~~ the range of values derived in previous literature works (Hock, 2003). ~~The limitations of this approach will~~
~~be diseussed in Section ??.~~ $DD_{t-1,t}$ is the DD given by the cumulative sum of the hourly temperatures exceeding a certain
 threshold:

$$DD_{t-1,t} = \sum_{h=t-1}^t T_h \text{ if } T_h > \hat{T} \quad (2)$$

400 The threshold temperature \hat{T} is set to $0^{\circ}C$.

The DD is first calculated for each station and then spatially interpolated using a three-dimensional universal kriging routine
 with linear variogram and ~~elevation as~~ external drift (Murphy et al., 2020). The choice arises from the results of a leave one
 out (LOO) ~~cross-validation~~ ~~cross-validation~~ (see Appendix B). The variogram parameters are automatically calculated at each
 time step using a "soft" L1 norm minimization scheme. The number of averaging bins is set ~~as to~~ 6 (default value). The kriging
 405 is performed on the daily DD values instead of on the raw hourly temperature values to reduce computational times.

We can determine the total amount of melting M_{tot} by summing ~~up all the all~~ daily $M_{t-1,t}$ for all those days in *ablation*
 within the time range $[t_{SA}; t_{SD}]$. It is worth noting that a single pixel may have more than one ~~single~~ snow period, ~~and~~ hence
 we can have more than a couple of $t_{SA}-t_{SD}$. M_{tot} , which has to be equal ~~to~~ the total accumulation A_{tot} , is then calculated as
 follows:

$$410 \quad A_{tot} = M_{tot} = \sum_{t=t_{SA}}^{t_{SD}} M_{t-1,t} \text{ if } \textit{ablation} \text{ for } t \quad (3)$$

Consequently, it is possible to reallocate the total accumulation on ~~those days which days that~~ are in *accumulation*:

$$A_{t-1,t} = k_{t-1,t} A_{tot} \text{ if } \textit{accumulation} \text{ for } t \quad (4)$$

where $k_{t-1,t}$ is a coefficient that represents the ~~quantity of the snowfall. In case~~ amount of snowfall. If we have a network made by ~~S AWS~~ AWSs with measured SWE (or similarly, SD), k is set proportional to the observed snowfalls:

$$415 \quad k_{t-1,t} = \frac{\sum_{s=1}^S (SWE_t^s - SWE_{t-1}^s)}{\sum_t \sum_{s=1}^S S(SWE_t^s - SWE_{t-1}^s)} \quad \text{if } \textit{accumulation} \quad \text{for } t \quad (5)$$

Note that the number of days in *accumulation* varies for each pixel ~~and consequently,~~ and consequently, the coefficient is a function of time and space. Thus, it is possible to determine the final output, i.e., a daily HR SWE time-series, by applying pixel-wise the following rules:

$$SWE(t) = \begin{cases} 0 & \text{if } \textit{snow-free} \\ SWE(t-1) & \text{if } \textit{equilibrium} \\ SWE(t-1) - M_{t-1,t} & \text{if } \textit{ablation} \\ SWE(t-1) + A_{t-1,t} & \text{if } \textit{accumulation} \end{cases} \quad (6)$$

420 It may happen that during *ablation* temperatures are low and the term $M_{t-1,t}$ is equal to 0, thus coinciding with the *equilibrium* state. ~~Note that M may also be greater than 0 but if the state is different from *ablation*, that melting is not encountered. It is in fact possible that temperatures present some inaccuracies or increase without causing a real melting. In other words, we assume that *ablation* is only possible when we have contemporary: i) absence of snowfalls, ii) a decrease of SAR backscattering, and iii) high temperature. The term $A_{t-1,t}$ is instead always positive.~~

425 It is worth stressing the fact that ~~even though possible redistribution caused by wind although sublimation, redistribution,~~ and gravitational transport ~~is are~~ is not explicitly taken into account in Eq. 6, ~~its their~~ its consequences are implicitly ~~appreciated by observing observed as~~ appreciated by observing observed as a longer persistence of snow on the ground. ~~Indeed, the potential melting is distributed over space and time by considering the snow cover duration. This implicitly takes into account the difference in the energy inputs due to both the topographic and the redistribution effects providing a good estimation of the total SWE that is detectable through the use~~ of an accurate SCA time-series. Moreover, by providing an approximation of the accumulation events, we also consider late snowfalls that ~~may can~~ may occur during the main melting season and that are a ~~large major~~ large major source of error in ~~the~~ state-of-the-art methods (Slater et al., 2013a).

3 Study Areas and Dataset Description

To assess the performance of the proposed method, we consider two different test areas. The first one is the South Fork ~~catchment of the San Joaquin River (SFSJR)~~ catchment of the San Joaquin River (SFSJR) located in California, USA, in the Sierra Nevada. For this test site, we considered three hydrological seasons ~~spanning from the 1st of that spanned from 1~~ spanning from the 1st of that spanned from 1 October 2018 to ~~30th of 30~~ 30th of 30 September 2021. The considered basin has an area of around 970 km² and a mean elevation of 3070 m, ranging from a minimum elevation of 1930 m ~~up~~ up to a maximum elevation of 4150 m. ~~For this catchment, a spatialized SWE product~~ For this catchment, a spatialized SWE product ~~The percentage of forest area in this catchment is around 32% (Shimada et al., 2014). SWE maps with a resolution of 50 m is available~~ The percentage of forest area in this catchment is around 32% (Shimada et al., 2014). SWE maps with a resolution of 50 m is available ~~acquired are made~~

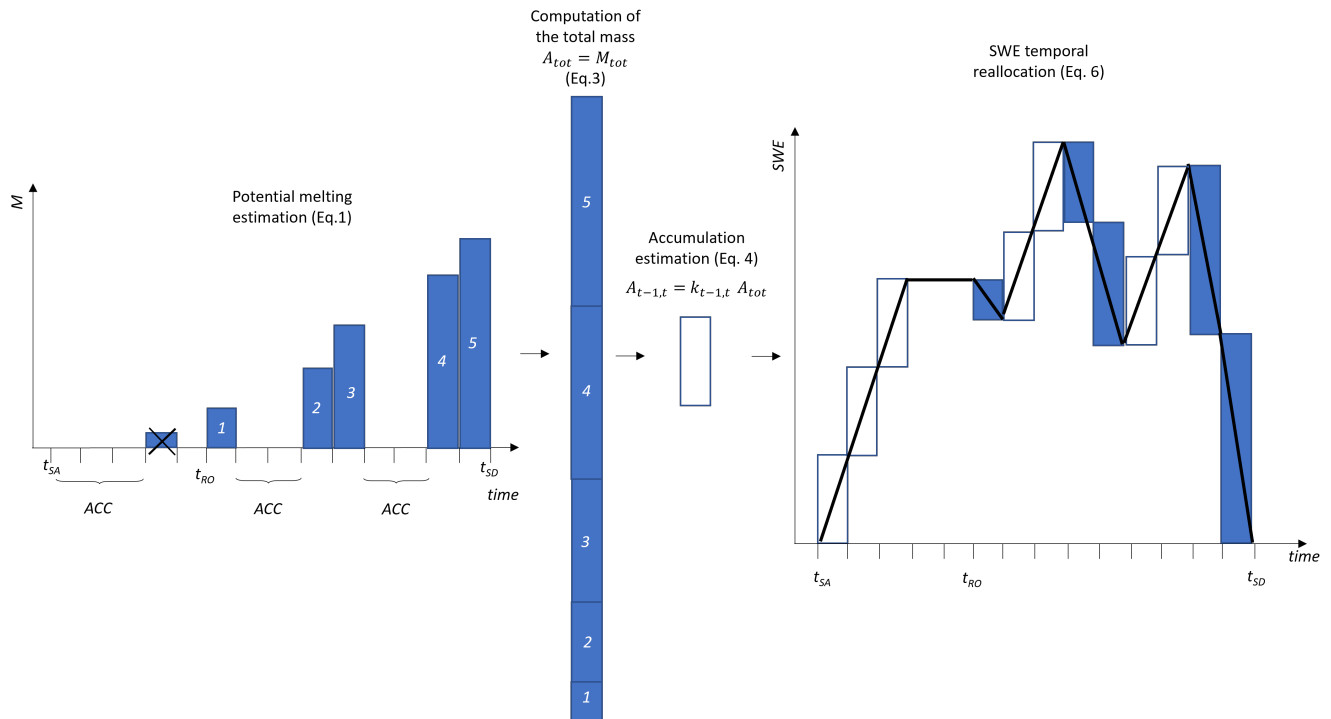


Figure 2. Illustration of the reconstruction and temporal reallocation of the SWE for a given pixel. Starting from the left side of the figure, the **catchment**-state is identified for each day of the snow season (delimited by t_{SA} and t_{SD}) and the potential melting is estimated according to Eq.1. Incorrect melting events prior to the runoff onset are excluded. The sum of all the potential melting at the different days represent the total amount of SWE for that pixel. This is redistributed during the *accumulation* day using Eq.4. For this illustrative example, a constant k is considered. As one can notice the reconstructed SWE can represent *accumulation* (even as late spring snowfall), *ablation* and *equilibrium* conditions.

440 available by the Airborne Snow Observatory (ASO). ASO couples an imaging spectrometer, ~~laser-scanner~~ a laser scanner, and a physical model that provides an estimate of the snow density to derive accurate SWE maps (Painter et al., 2016). ~~One~~ The product presents an uncertainty that derives from both the snow depth retrieval (< 0.02 m at a resolution of 50 m) and the snow density modeling ($13\text{--}30$ kg m $^{-3}$). This dataset represents our main reference for this study, given its high spatial detail comparable with the proposed output. However, we consider also an additional dataset at ~ 500 m resolution, i.e.,

445 the Western United States daily snow reanalysis (WUS-SR) product (Fang et al., 2022). A snow pillow for continuous SWE measurements and ~~one~~ an AWS providing air temperature are available~~inside~~. Unfortunately, this is the only station within the catchment. Moreover, we considered For this reason, as explained in Sec. 2.1 we assumed that the accumulation occurs across all the snow-covered area. However, we also considered other 6 snow pillows and 10 stations with continuous temperature measurements within a radius of ~~around~~ approximately 15 km from the catchment (see 3a). These data were downloaded from

450 the United States Department of Agriculture (USDA) Natural Resources Conservation Service (NRCS) Snowpack Telemetry

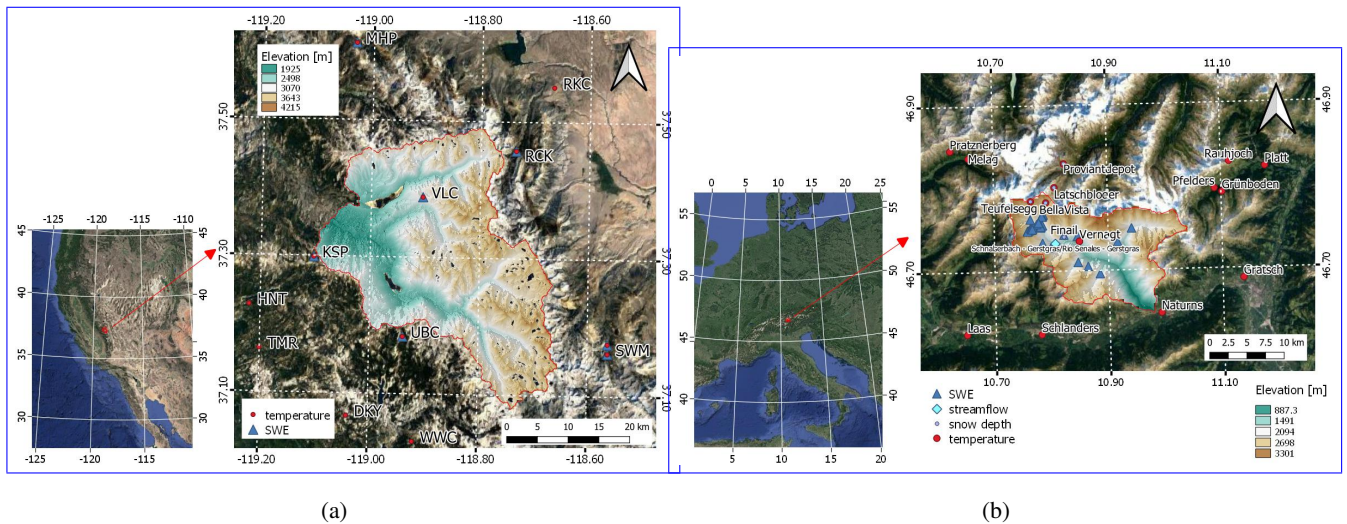


Figure 3. Overview of the two test sites: a) South Fork catchment of the San Joaquin River, California, USA, and b) Schnals catchment, South Tyrol, Italy. Background image ©Google Maps 2022.

(SNOTEL) network (see <https://www.wcc.nrcs.usda.gov/snow/>) and from the California Data Exchange Center (CDEC) (see <https://cdec.water.ca.gov/>).

The second catchment is the Schnals (Senales in Italian - for brevity we will report the German name only) located in the Vinschgau (Venosta) Valley in South Tyrol, ~~Italy,~~ (Italy) in the Alps. For this catchment, we analyzed two hydrological seasons spanning from ~~the 1st of 1~~ October 2019 to ~~the 30th of 30~~ September 2021. The considered area has an ~~extension of~~ about extent of approximately 220 km² and a mean elevation of 2370 m, ranging from a minimum ~~elevation~~ of 590 m up to a maximum ~~elevation~~ of 3550 m. ~~For this test site, manual~~ The percentage of forest area is around 25% for this catchment (Shimada et al., 2014). Manual SWE measurements are available for the hydrological season 2020/21 (collected by Avalanche Centre ~~the Avalanche Center~~ of the Bolzano Province - Lawinenwarndienst - see <https://lawinen.report/weather/snow-profiles> - and by Eurac Research, Institute for Earth Observation). Additionally Furthermore, we considered the operating temperature and SD sensors of the Province of Bozen (see <https://data.civis.bz.it/it/dataset/misure-meteo-e-idrografiche>). An overview of the Schnals catchment and the location of available measurements is provided in Fig. 3b.

The HR daily SCA time-series is derived through using the method proposed by Premier et al. (2021). The input data used for the reconstruction are the S2, Landsat-8 and MODIS data. The method requires as input a long time-series of HR images. Hence Therefore, we downloaded a total of around about 400 scenes for ~~the South Fork catchment~~ SFSJR and 700 scenes for ~~the Schnals valley~~ Schnals from <https://earthexplorer.usgs.gov>. The following steps are applied to opportunistly ~~pre-processed~~ preprocessed the data: i) conversion from digital number to Top of the Atmosphere (ToA) reflectance values, ii) cloud masking through the algorithm s2cloudless available at <https://github.com/sentinel-hub/sentinel2-cloud-detector> (Zupanc, 2017), iii)

SCF detection through an unsupervised statistical learning approach (~~?~~)[\(Barella et al., 2022\)](#) (RMSE of 22.82 and an MBE of 6.95), and iv) binarization of the classification results –

~~The daily (SCF>10%). Daily~~ MODIS data are needed for ~~those hydrological seasons in analysis only~~ [the analyzed hydrological seasons](#). The ready-to-use MOD10 version 6.1 are distributed by the National Snow and Ice Data Center (see <https://nsidc.org/data/MOD10A1>) (Hall and Riggs, 2021). The NDSI values are converted to SCF by using the algorithm proposed by Salomonson and Appel (2004). [The output is a daily SCA time-series with a spatial resolution of 25 m.](#)

475 The S1 data are downloaded from <https://search.asf.alaska.edu/> and pre-processed (i.e., precise orbit application, thermal noise removal, border noise removal, beta ~~nought-naught~~ calibration, tile assembly, co-registration, multi-temporal filtering, terrain correction, geo-coding ~~and sigma nought~~, and [sigma naught](#) calibration). These steps are performed using SNAP (Sentinel Application Platform) and some custom tools. [The images are also resampled at 25 m using the same spatial grid as for the SCA maps.](#) Three tracks are available for each test site, i.e. track 64, 137, and 144 for the ~~South Fork catchment~~ [SFSJR](#) 480 and track 15, 117, and 168 for ~~the Schnal catchment~~ [Schnals](#), with a total number of around 480 and 350 downloaded images ~~respectively. The backscattering is then daily interpolated, respectively. For this work, we considered the VV polarization only, which is more suitable for runoff onset identification (Marin et al., 2020). The temporal resolution of each separated track is 6 days. For this reason, the backscattering is daily interpolated,~~ and a multi-temporal analysis is carried out for the three tracks separately. If at least one track shows a drop of at least 2 dB in the signal (Nagler and Rott, 2000) w.r.t. a moving 485 average of the 12 previous days, ~~that day we look for the minimum after the drop and for this moment onward the pixel~~ is considered to be in *ablation*.

4 Experimental Results

In this section, we present the results obtained for ~~the South Fork and for the Schnal catchment~~ [SFSJR and for Schnals](#).

4.1 South Fork ~~catchment~~ [of the San Joaquin River](#)

490 The proposed SWE maps are aggregated at a resolution of 50 m and compared ~~with to~~ the corresponding ASO maps, for a total ~~number~~ of 12 dates.

~~From a qualitative inspection of the results, a general good agreement between the two SWE maps is visible. For sake of brevity we propose here a detailed analysis of the 9th of June 2019, for which we reported in Fig. 6 the SWE map obtained with the proposed approach, the SWE produced by ASO and the bias map calculated as pixel-wise difference between the proposed and the reference ASO map. In general, it is possible to notice that the proposed method is able to reproduce spatial patterns similar to the ones detected by ASO. This result shows that the use of HR input data achieve an unique spatial detail, which represents one of the main advantages of the proposed method. By looking at a zoomed area, it is possible to better appreciate this similarity. Nonetheless, it is possible to notice a tendency of the proposed product to underestimate SWE especially in some North exposed areas. This may be due to either i) an error introduced by the DD model, that only considers temperature~~

500 without accounting for radiation differences linked to different exposures or ii) an error introduced by the reference SD map used in the ASO for defining the amount of snow at the beginning of the season in permanently snow covered areas.

Proposed SWE map (on the left), ASO SWE map (in the centre) and bias map calculated as difference between the proposed and ASO SWE (on the right) for the 9th of June 2019. A zoom is shown under the correspondent maps. A transect is shown with three green dots in the North area of the catchment. Background image ©Google Maps 2022.

505 SWE temporal trends for: the proposed approach (continuous lines) and ASO (crosses) for the considered transect reported in Fig. 6.

In Fig. 8 the temporal trend of three points for a selected transect is reported. First of all, it is possible to observe that the proposed product presents an expected behaviour, i.e., longer snow persistence and increasing SWE for higher elevation. On the other hand, ASO shows higher SWE for the mid elevation point. It is worth noting that even though we use ASO as
510 reference product, some inconsistencies may be present due to a possible inaccurate estimation of the snow density by the model.

The Volcanic Knob (VLC) monitoring site, which is located inside the analyzed area, is also used for evaluating the obtained results showing a very good agreement (see Fig. 5). Note that the first year Furthermore, we also compare the results with the daily Western United States snow reanalysis (WUS-SR) dataset at 500 m provided by Fang et al. (2022). The results of the
515 intercomparison with ASO are reported in Table 2. The analysis shows a good correlation between the two products, with an average correlation coefficient of 0.740. The average bias is -22 mm, the average percent bias (PBIAS) is -19%, and the average RMSE is 212 mm. Our SWE maps underestimate the SWE compared to ASO for the first two seasons, 2018/19 is also used to set up the constant and 2019/20, while overestimating it for 2020/21, which was the driest season with SWE below average (see Appendix A Fig. A1). A possible explanation is that a drier season leads to earlier melting. As the DD method does not
520 consider seasonality in the DD factor ~~caused for the DD model, according also to values found in literature (Hoek, 2003).~~ The validity of the chosen value is confirmed by a good agreement of the results for the following two seasons. Interestingly, even though the stations are used to identify the *accumulation* state the temporal SWE trend does not necessarily present everywhere the same shape as for the station (see in Fig. 8 and 5). In fact, this final result is influenced also by the persistence of the snow as well by the potential melting, that varies depending especially by the elevation as it is calculated with a kriging with external
525 drift. Hence, the good agreement with the station trend is also confirming the validity of the proposed method.

SWE obtained by the proposed approach (in orange) against the measured SWE (in blue) at the Volcanic Knob test site for the hydrological seasons a) 2018/19, b) 2019/20 and c) 2020/21.

The results of a quantitative global analysis are reported in Table 2. The evaluation shows a generally good correlation between the two products, i.e., 0.729 on average. The average bias is -40 mm and the average RMSE is 216 mm. The highest
530 bias and RMSE values are generally encountered in the it is possible that we overestimate the potential melting during the first phase of the season when melting rates are lower due to less energy radiation input (Musselman et al., 2017; Ismail et al., 2023). Additionally, the five SWE maps from the first season, 2018/19, show decreasing RMSE values from mid-winter acquisitions. This is due to the fact that the snow cover in that period of the year is higher, and consequently the SWE, thus generating a potential larger error. Moreover, it is possible to have an inaccurate detection of the exact location and duration of the

535 snowfalls. This may be due to the fact that the accumulation in the proposed method is driven by punctual measurements and may be not representative of the entire catchment as described in Sec. 2.1. For the South Fork area, only one station is inside the catchment and this is not enough to capture the high variability of precipitations as expected to late-summer acquisitions. Larger errors during the mid-winter season (around the maximum SWE) are probably due to error propagation (Slater et al., 2013b; Rittger et al., 2016).

Table 2. Results of the ~~comparison~~ intercomparison between the proposed SWE and ASO ~~products~~ maps for the SFSJR. Bias, RMSE, and correlation are calculated pixel-wise, ~~while SWE tot is calculated for the SWE integrated over space~~ while SWE tot is calculated for the SWE integrated over space whole basin.

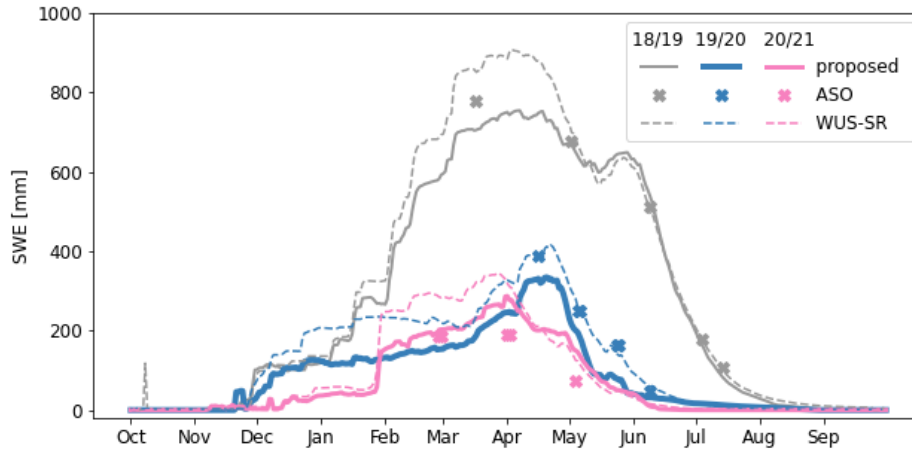
Date	BIAS [mm]	PBIAS [%]	RMSE [mm]	Correlation [-]	SWE tot-ASO [Gtmm]	SWE tot-proposed [Gtmm]
17 <u>2019/03/2019-17</u>	-88 <u>-82</u>	311 <u>-11</u>	<u>315</u>	0.73	734 <u>778</u>	653 <u>699</u>
02 <u>2019/05/2019-02</u>	-66 <u>-33</u>	308 <u>-5</u>	<u>299</u>	0.84	640 <u>679</u>	580 <u>647</u>
09 <u>2019/06/2019-09</u>	-71 <u>-7</u>	299 <u>-1</u>	0.86 <u>268</u>	482 <u>0.88</u>	417 <u>511</u>	<u>504</u>
04 <u>2019/07/2019-04</u>	-59 <u>-37</u>	197 <u>-24</u>	0.85 <u>185</u>	167 <u>0.86</u>	113 <u>177</u>	<u>143</u>
14 <u>2019/07/2019-14</u>	-51 <u>-41</u>	166 <u>-58</u>	<u>164</u>	0.80	100 <u>106</u>	53 <u>67</u>
15 <u>2020/04/2020-15</u>	-70 <u>-71</u>	239 <u>-21</u>	0.64 <u>242</u>	367 <u>0.63</u>	303 <u>389</u>	<u>321</u>
05 <u>2020/05/2020-05</u>	-65 <u>-53</u>	225 <u>-26</u>	0.66 <u>224</u>	235 <u>0.67</u>	165 <u>250</u>	<u>199</u>
23 <u>2020/05/2020-23</u>	-95 <u>-91</u>	234 <u>-112</u>	<u>235</u>	0.65	156 <u>166</u>	69 <u>78</u>
08 <u>2020/06/2020-08</u>	-20 <u>-18</u>	152 <u>-58</u>	<u>161</u>	0.66	44 <u>48</u>	26 <u>30</u>
26 <u>2021/02/2021-26</u>	-8 <u>-12</u>	130 <u>-6</u>	0.65 <u>125</u>	175 <u>0.67</u>	167 <u>186</u>	<u>198</u>
31 <u>2021/03/2021-31</u>	59 <u>-81</u>	<u>29</u>	168	0.70 <u>0.73</u>	180 <u>191</u>	235 <u>271</u>
03 <u>2021/05/2021-03</u>	49 <u>-74</u>	166 <u>-50</u>	0.70 <u>160</u>	67 <u>0.80</u>	123 <u>-72</u>	<u>145</u>

540 In Fig. 4, the temporal trend of the total SWE for the three considered hydrological seasons is shown. We notice a general ~~good agreement between~~ Similarly, Table 3 presents the results of the comparison between the proposed SWE dataset and the WUS-SR dataset, where metrics are computed pixel-wise by aggregating the proposed SWE at a 500 m resolution. An average value is then computed for the entire season. The comparison reveals a systematic negative bias, which may be attributed to the different modeling of snow under canopy. The correlation between the proposed and WUS-SR datasets is lower than that
545 between the proposed and ASO datasets. For further comparison, Appendix C includes additional analyses of the proposed approach, WUS-SR, and ASO at a 500 m resolution. The analysis shows that the WUS-SR dataset also correlates worse with ASO. However, the three time-series show a consistent behaviour.

Good agreement is also confirmed when comparing the total amount of SWE estimated through the ~~two approaches~~ . The plot also gives an idea of the large differences that can be encountered three approaches in the catchment. Fig. 4 shows
550 the time-series of the total SWE for the three hydrological seasons. In the plot, it is possible to appreciate the large SWE variability that can occur for different seasons and that ~~are well captured by the proposed method~~ is well represented by all three time-series. The first hydrological season 2018/2019-19 shows the highest amount of SWE, while the others are drier. The tendency is of a slight underestimation of SWE for the proposed method w. r. t. ASO results for the first two seasons, while

Table 3. Results of the intercomparison between the proposed SWE and WUS–SR for the SFSJR. Bias, RMSE, and correlation are calculated pixel-wise. The proposed SWE was aggregated to 500 m resolution.

Season	BIAS [mm]	PBIAS [%]	RMSE [mm]	Correlation [-]
2018/19	-51	-22	174	0.73
2019/20	-51	-40	108	0.63
2020/21	-31	-25	100	0.63



Temporal trends of the total SWE for the South Fork catchment over the three analyzed seasons. Crosses represent the ASO reference

Figure 4. Time-series of the total SWE for the SFSJR over the three analyzed seasons. Continuous lines represent the proposed time-series, dashed lines the WUS–SR dataset, and crosses represent the ASO reference.

the last is overestimated as also shown in Table 2. The possible reasons will be discussed in Sec. 5. For reference, the SWE regime for the catchment is reported in Fig. A1 in Appendix A.

The Volcanic Knob (VLC) monitoring site, which is located within the analyzed area, is also used to evaluate the obtained results, and it shows good agreement between the proposed time-series and the in-situ measurements (refer to Fig. 5). Note that the WUS-SR presents a delay in detecting the t_{SD} probably due to the coarser resolution, i.e., 500 m, despite a similar trend. It is worth noting that the first year, 2018/19, is also used to set up the constant a used for the DD model, in accordance with values found in the literature (Hock, 2003; Ismail et al., 2023). The validity of the chosen value is confirmed by the good agreement of the results for the next two seasons. However, a delay in detecting t_{RO} is observed in season 2018/19 that results in a smaller SWE peak.

A We also propose here a more detailed analysis is presented in Fig. ??, where we show the trend of on a specific date. To keep this analysis concise, we propose to consider a date during the full melting season, a period of particular interest from

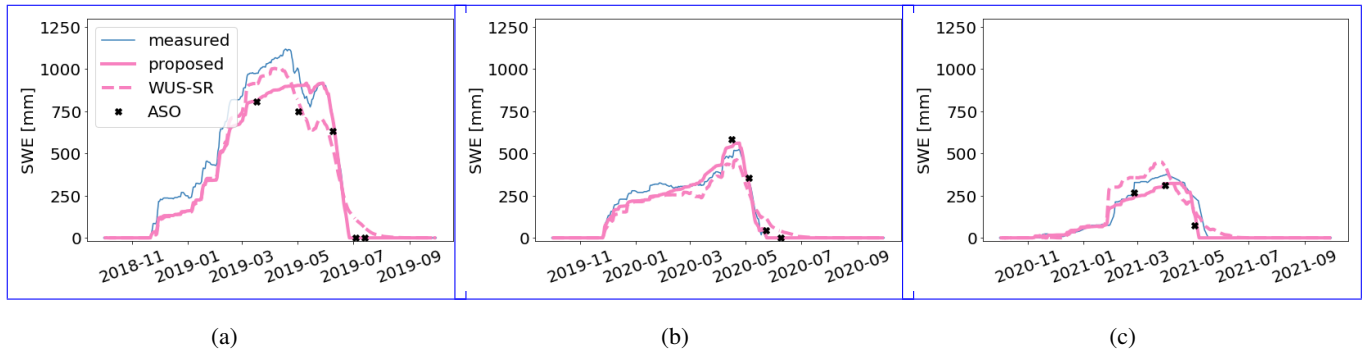


Figure 5. SWE obtained by the proposed approach (pink continuous line) is compared against the measured SWE (in blue), the WUS-SR SWE (pink dashed line), and ASO SWE (black crosses) at the Volcanic Knob test site for the hydrological seasons a) 2018/19, b) 2019/20, and c) 2020/21. To extract SWE at the considered location, the original spatial resolution of each dataset is maintained.

565 a hydrological perspective. The considered date is the ~~maximum of SWE versus~~ 9 June 2019. For the analysis on the other
 570 ~~dates and the intercomparison with the WUS-SR dataset, please refer to the Appendix C. Fig. 6 reports the proposed SWE~~
~~map, the ASO SWE map and the bias map calculated as the pixel-wise difference between the proposed and the reference ASO~~
~~map at 50 m. In general, it is possible to notice a good agreement between the two maps. The proposed method is capable~~
~~of reproducing spatial patterns similar to those detected by ASO. This finding demonstrates that the use of HR input data~~
 575 ~~achieves a unique spatial detail, which represents one of the main advantages of the proposed method. Upon closer inspection~~
~~of a specific area, this similarity can be better appreciated. Nevertheless, it is possible to notice a tendency of the proposed~~
~~SWE maps to underestimate SWE especially in some areas exposed to the north. This could be attributed to either i) an error~~
~~introduced by the DD model, which only considers temperature and may not account for radiation differences associated with~~
~~different aspects (Ismail et al., 2023), or ii) an error in the snow depth retrieval or snow density modeling introduced in the~~
~~ASO maps.~~

Fig. 7a displays the mean SWE values for different elevation, slope and aspect. ~~The results show an increasing trend of~~
~~SWE with elevation that is inverted for highest quotes, since these usually present~~, and aspect ranges. The most significant
 580 ~~changes are observed when analyzing the different elevation ranges. The trend is quite consistent, with an increase in SWE as~~
~~elevation increases up to approximately 3500 m a.s.l., while the trend is reversed for higher elevations. These areas generally~~
~~have very steep slopes and consequently, resulting in a marked tendency of for snow to be subjected subject~~ to gravitational
 transport. ~~This is also confirmed by the second graph, where steeper slopes present less SWE. Another coherent result is also~~
~~the bigger~~ The two SWE maps only differ for elevations higher than about 4100 m a.s.l., where the proposed SWE starts to
 585 ~~increase again, while the ASO continues to decrease. The slope analysis shows larger differences, especially when considering~~
~~steep slopes. The proposed method underestimates SWE compared to ASO. We generally expect lower SWE for these steeper~~
~~slopes that promote gravitational transport. The aspect analysis correctly indicates a larger amount of SWE for North exposed~~
~~areas. These results confirm that the method is suitable to be exploited for hydrological applications. north-facing areas. As~~

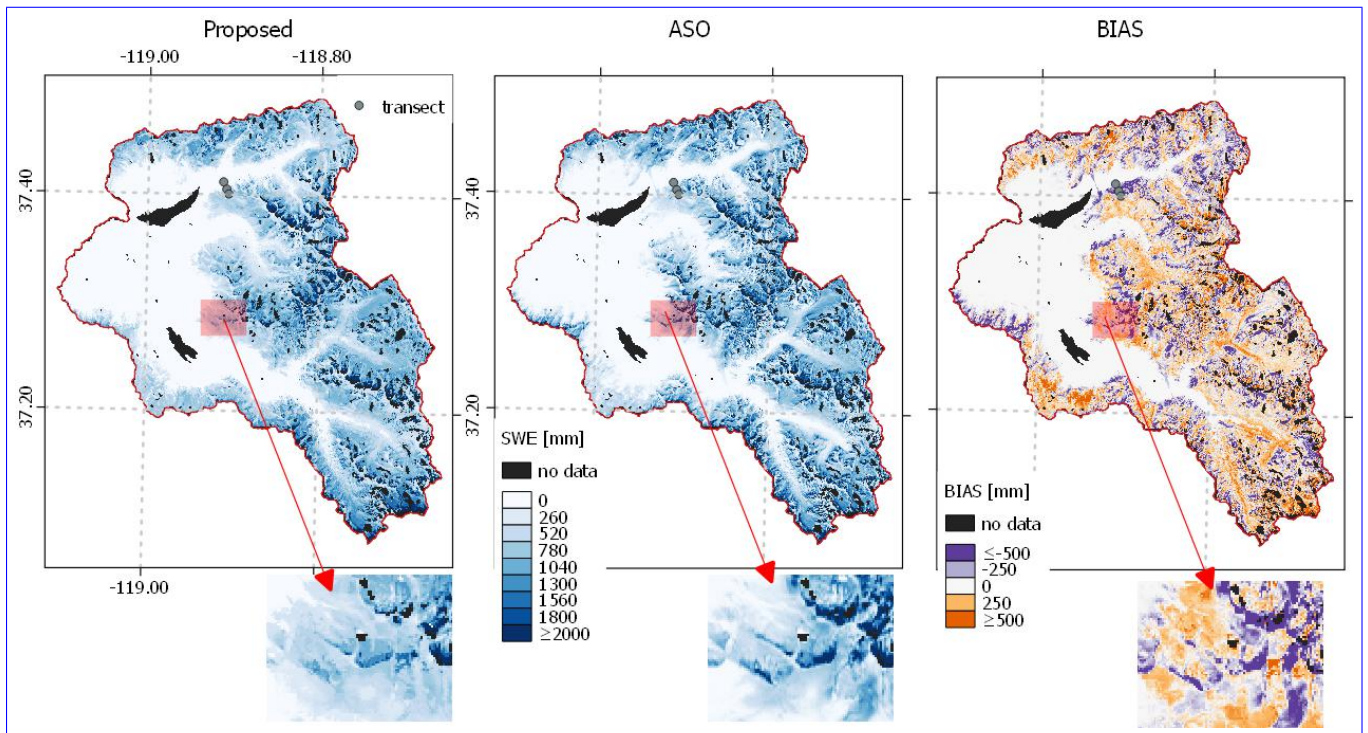


Figure 6. Proposed SWE map (on the left), ASO SWE map (in the centre) and bias map calculated as difference between the proposed and ASO SWE (on the right) for the 9 June 2019 for the SFSJR. A zoom is shown under the correspondent maps. A transect is shown with three green dots in the North area of the catchment.

mentioned earlier, we can observe an underestimation of the SWE for north-facing slopes when comparing our maps with the ASO. Conversely, we would expect an overestimation of the SWE for the north-facing areas, as the DD method does not consider radiation effects. However, we never observe this overestimation when considering this and other available reference dates presented in Appendix C.

For more results derived by the comparison between Fig. 7b shows the dispersion graph for the proposed method and the ASO reference product we refer the reader to the Appendix C-ASO. In general, a strong correlation can be observed, albeit with significant dispersion, which is also confirmed by the computed correlation and RMSE value reported in Table 2. However, the majority of the points are clustered around the diagonal line.

Fig. 8 shows the time series for the 2018/19 season for three points along a selected transect (see Fig. C1). Here we report a detailed analysis on the total SWE for all the available ASO SWE information considering different elevation-, aspect and slope belts (see Fig. C3 and ??). 6 for their location). It is possible to observe that the proposed SWE presents the expected behavior, i.e., longer snow persistence and increasing SWE for higher elevation. Despite some differences that can be due to the different spatial resolution between the two products, this trend is respected also for the WUS-SR dataset. On the other hand,

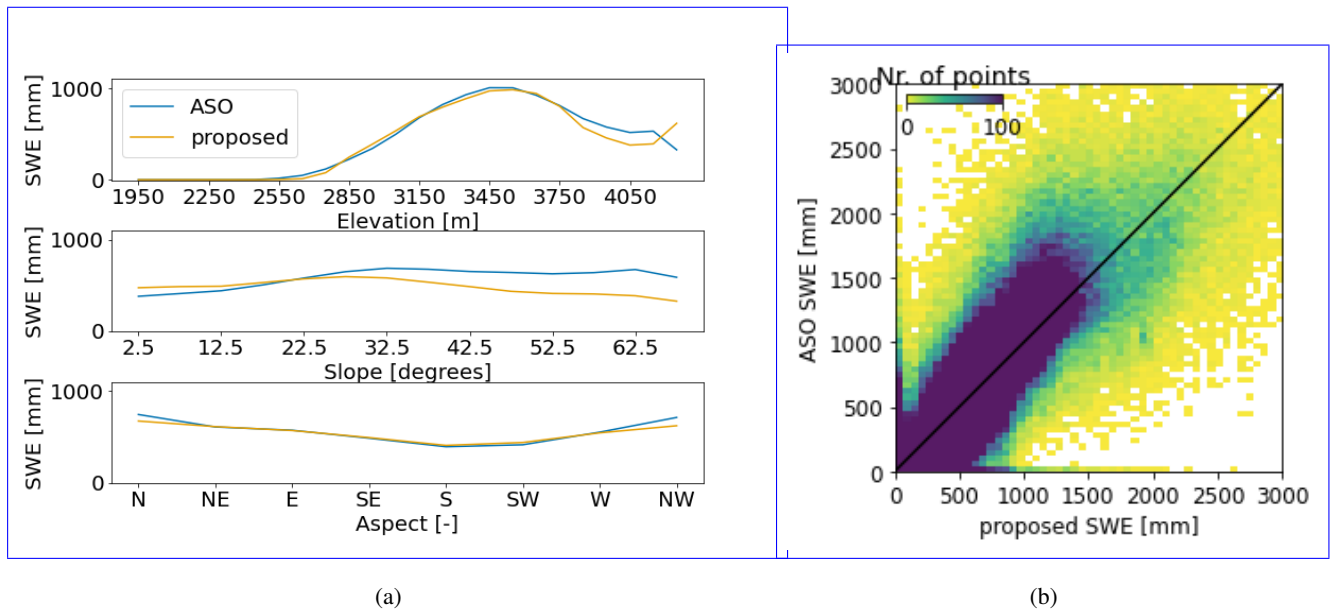


Figure 7. Mean SWE value for different elevation, slope and aspect belts (on the left). The proposed SWE (in orange) is evaluated against ASO (in blue) for the 9 June 2019 for the SFSJR. On the right, dispersion graph for the same date.

the ASO shows a higher SWE for the mid elevation point. Note that even though we use ASO as a main reference, there may be inconsistencies present, such as possible inaccurate estimation of the snow density by the model. Interestingly, the figure also correctly shows a variability in the three proposed SWE time-series. Notwithstanding the stations are used to identify the accumulation state, the SWE time-series does not necessarily present the same shape everywhere as for the station (see Figs. 8 and 5). The final result is influenced not only by the persistence of the snow, but also by the potential melting, which varies depending on the elevation. This is calculated using kriging with external drift.

4.2 Schnals catchment

For the Schnals valley, reference spatialized data of SWE are spatialized SWE data to be used as reference are unfortunately not available. However, manually collected manual SWE measurements for the hydrological season 2020/21 were collected also along spatial transects. For more details about the measurement location, please refer to the Appendix A, Fig. ?? The location of the measurements is shown in Fig. 3b. The results show a bias of 38 mm and a RMSE of 209 mm, indicating a general good agreement. For sake of brevity, we report in Fig. ?? only few examples of reconstructed SWE evaluated -5 mm, an RMSE of 191 mm, and a correlation of 0.35. Fig. 9 shows the proposed reconstructed SWE plotted against the manual measurements. It is possible to notice, in accordance with the results obtained for the South Fork catchment, that the variability from an area to another of the catchment is properly caught by the proposed method. This is due to the different persistence of snow on ground that modulates the spatial variability of the potential melting estimated by the DD model. It is possible to notice in the figure

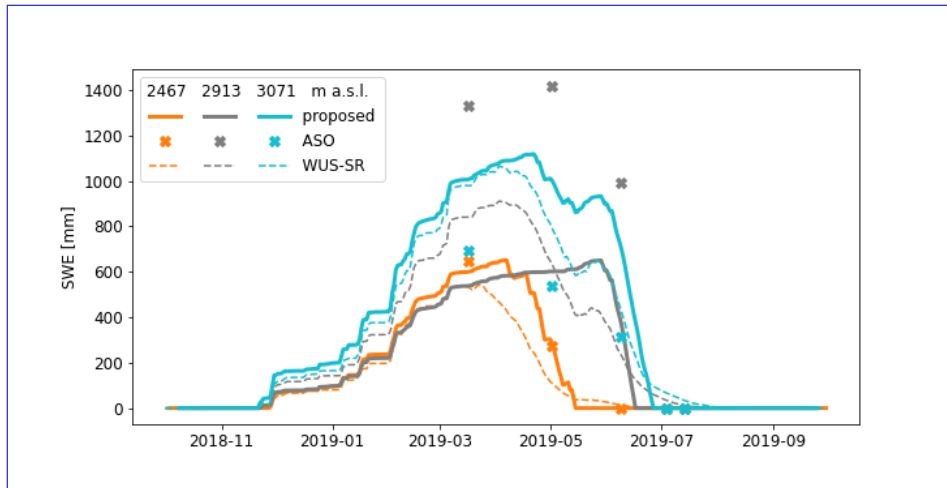


Figure 8. Trends of the maximum of SWE time-series in 2018/19 for the hydrological seasons 2018-2021 w.r.t. the elevation proposed approach (upcontinuous lines), slope WUS-SR (centredashed lines) and aspect ASO (lowcrosses) for a transect in the South Fork catchment SFSJR reported in Fig. 6. To extract SWE at the considered locations, the original spatial resolution of each dataset is maintained.

that the SWE tends increases with Despite a generally good agreement, we observe some significant differences and a worse performance compared to the analysis performed for the Californian catchment. However, the elevation reference dataset is insufficiently informative and represents only a few points that may not be entirely representative of the intra-pixel variability, especially in complex terrains. As shown by the SWE measurements acquired in Schnalstal by Warscher et al. (2021), a high spatial heterogeneity of the SWE can be encountered when considering a pixel with a size of 25 m. This results in inherent difficulties in appropriately evaluating the output.

In Fig. 10 we report shows the map of the SWE maximum maximum SWE for the two analyzed hydrological seasons. It From these highly detailed maps, it is possible to see that the season 2020/21 is characterized by a higher amount of SWE. However, the two years show similar patterns that are coherent consistent with the morphology of the study area. In detail, we can notice that interestingly there is a higher amount of SWE especially in the East part of the catchment that corresponds to the glacierized area of the Roteck/Monte Rosso mountain. We found a longer persitenee persistence of snow for these North exposed slopes and consequently a larger amount of reconstructed SWE. The consistency of the SWE patterns is also confirmed by Fig. ??, from which similar considerations as for the South Fork catchment can be carried out. Another qualitative indicator of the goodness of the results is given in Fig. ?. The trend of the SWE maximum over time is represented together with the discharge measured at Schnalserbach

Due to the absence of an appropriate dataset for the SWE intercomparison in the Schnals valley, we carry out a qualitative analysis of the correlation between SWE and riverine discharge. To achieve this, we analyze i) the discharge measured at Schnalserbach - Gerstgras. In the second year, higher SWE amounts correspond to a higher peak in terms of measured discharges expected. Moreover Gerstgras; ii) the SWE variations that are associated with runoff (i.e., only when they are

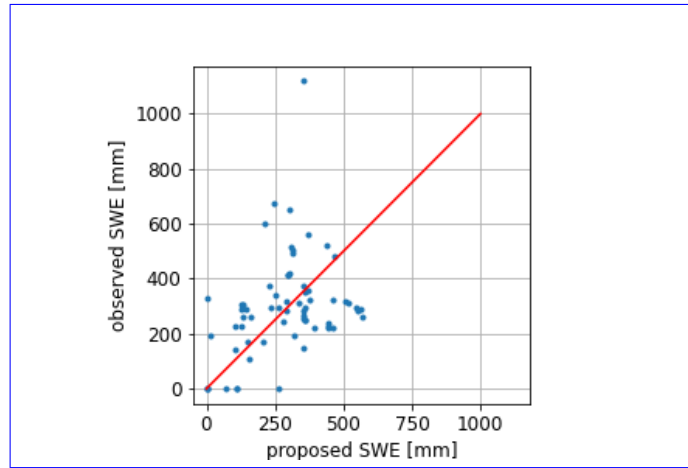


Figure 9. Proposed SWE proposed (continuous line x-axis) against the manual-measured-observed SWE (crosses y-axis) at some locations for the season 2020/21 in the Schnals catchment (see Fig. 223b).

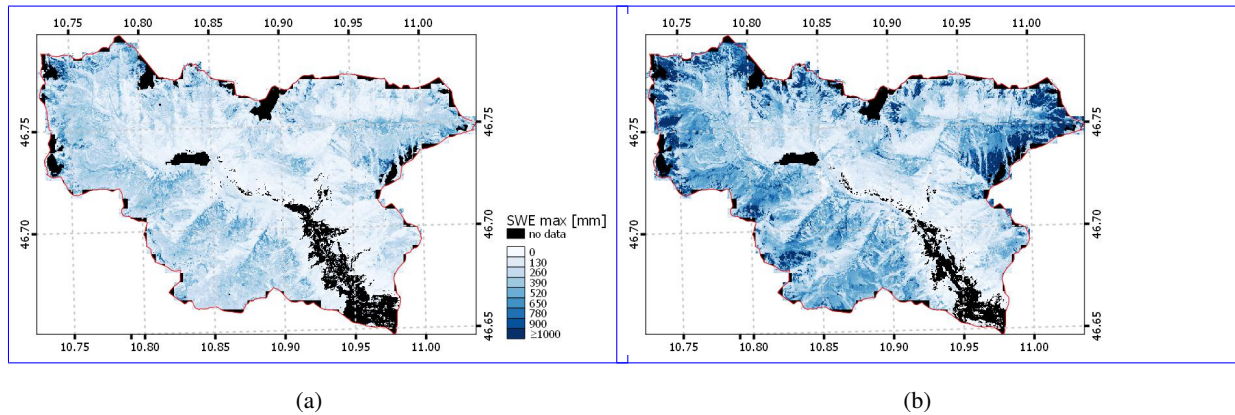


Figure 10. Maximum of SWE for the Schnals catchment for the hydrological seasons a) 2019/20 and b) 2020/21.

associated with a decrease in SWE) for the corresponding subcatchment, and iii) the precipitation measured at Vernagt. Refer to Fig. 3b for the location of the outlet point and pluviometer. Fig. 11 shows good agreement in terms of both timing and quantity between snow-generated runoff and discharge, confirming that the catchment is snowmelt dominated. The discharge starts increasing in correspondence with the snowmelt, and it starts decreasing when the snowmelt is reduced for both periods.

640 The first year shows a delay, while the response is more direct for the second season. More than differences in terms of precipitation, we ascribe this situation to a different snowmelt rate. Indeed, the season 2019/20 shows an earlier, weaker, and longer distributed snowmelt period, interrupted by periods with low SWE output (such as the end of March-beginning of April, beginning of May, or middle of June). This situation may favor ground infiltration with a predominance of subsurface runoff w.r.t. surface runoff, contributing slowly to the discharge. On the other hand, the 2020/21 season shows a long and high

645 intensity SWE release (end of May-end of June) that may cause a sudden saturation of the soil, with predominant surface runoff contributing more directly to the discharge. This hypothesis may also be confirmed by recent literature, showing that when snowmelt is earlier, it is possible to appreciate for the two seasons an increase of discharge that happens in correspondence of the SWE decrease also less intense, and the runoff response could be reduced, with strong implications for future climate change impacts (Musselman et al., 2017). However, other contributions should also be considered, such as the storage of water

650 in the two reservoirs present in the territory. While a proper analysis requires a complete hydrological study and a hydraulic characterization of the watershed properties, we believe that this simplified analysis demonstrates the potential of the presented results in a real application.

5 Discussion

~~We have presented in the previous section the quantitative and qualitative results for the two study areas. Notwithstanding the good agreement with the observed measures as well as with the reference ASO product, we will draw in this section a critical~~

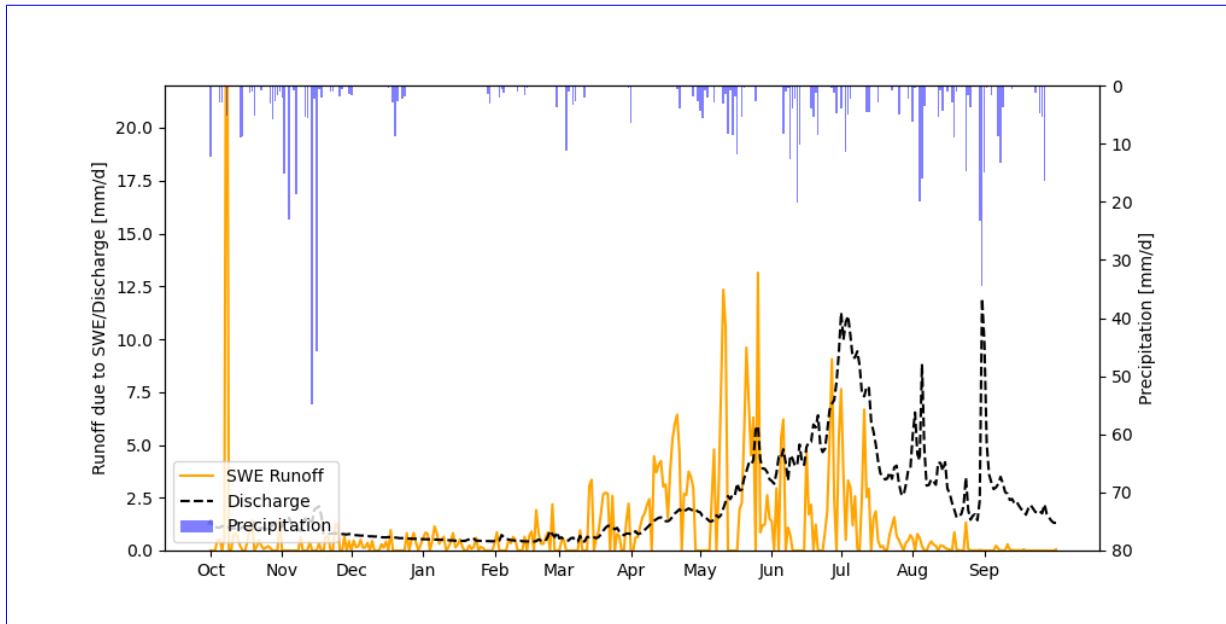
655 ~~The results indicate that the proposed method is capable of reproducing the SWE with high geometrical detail and in an accurate way. Particularly good agreement w.r.t. other datasets is achieved when considering the results on a catchment scale. The method demonstrates good performance in reproducing the expected SWE behavior when analyzing the topography of the study area. However, when considering a reference with comparable spatial resolution, significant differences are observed.~~

660 ~~In this section, we discuss the main sources of errors and weaknesses that may affect the results and provide a simplified sensitivity analysis of the parameters that play a role in the proposed approach. In detail, each main step, i.e., catchment~~

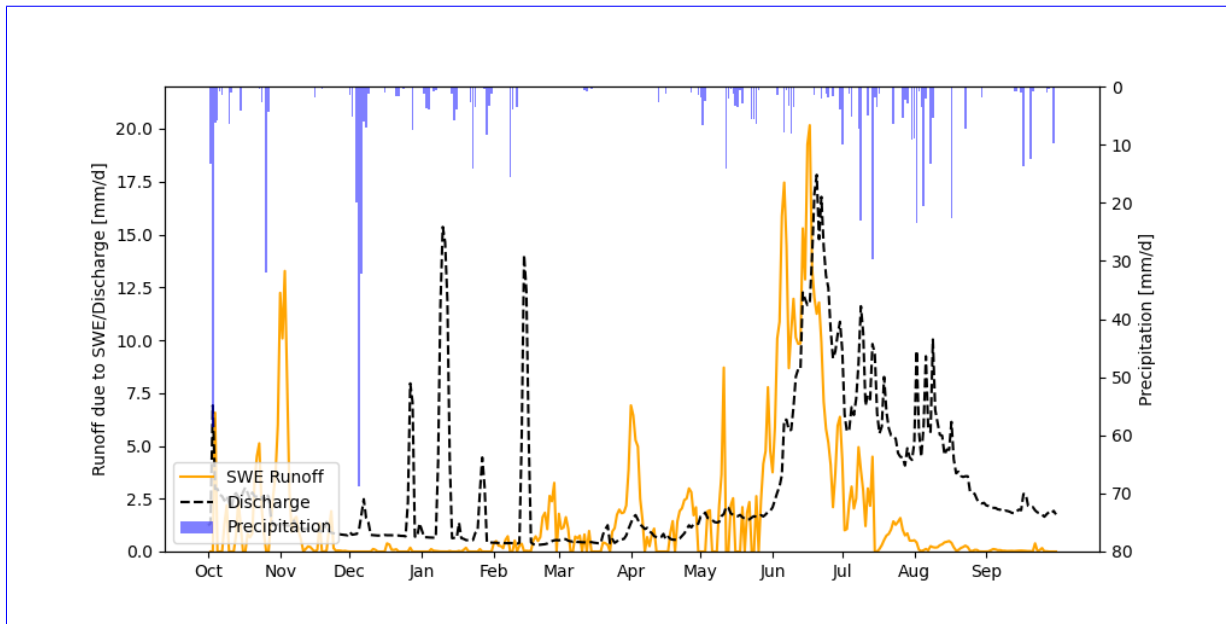
Furthermore, we also provide a detailed discussion of the effectiveness of the novel SCA regularization introduced through the state definition.

5.1 Sensitivity analysis

665 The potential sources of errors in the method are represented by i) a wrong state identification, SCA regularization and SWE reconstruction, is analysed in the following paragraphs, focusing on the main sources of errors.



(a)



(b)

Figure 11. Maximum of SWE–Snow generated runoff (in orange), discharge (dashed black line) and precipitations (in blue) for a subcatchment in the Schnals catchment valley closed at Schnalserbach - Gerstgras (see Fig. 3b) for the hydrological seasons: a) 2019/20 and b) 2020/21. Black areas represent glaciers that are masked out ©Randolph Glacier Inventory (RGI 6.0).

Trends of the maximum of SWE for the hydrological seasons 2019–2021 w.r.t. the elevation (up), slope (centre) and aspect (low) for the Schnals catchment:

SWE for the Schnals catchment for the hydrological seasons 2019–2021. Continuous lines represent SWE, dashed lines represent the discharge measured at Schnalserbach – Gerstgras.

5.2 Error in the determination of the catchment state

In Sec. 2.1 we have described how to define the *accumulation* state starting from in-situ SWE, SD or precipitation measurements. We suggested that a network of AWS is needed to cope with the possible heterogeneity of ii) the incorrect identification of t_{SA} and t_{SD} , which in turn depends on the accuracy of both the SCA time-series and the state, and ii) the use of a DD model for the potential melting estimation, which in turn depends on the goodness of the snowfalls inside the catchment. However, we would like to discuss more in detail the topology of such a network. In Sec. 2.1 we assumed that the *accumulation* state refers to all the catchment covered by snow without distinguishing between areas that are interested by a snowfall and areas that are in *equilibrium* or *ablation*, e.g., this is the case of contemporary rain-on-snow and snowfall inside the catchment. We introduced this simplifying hypothesis since temperature data, the interpolation routines, and the simplified assumption of the method itself, which does not take into account different energy inputs due to either topographical features or different periods of the year. Since the input data are subject to several degrees of preprocessing, it is difficult to precisely determine where the snowfall occurs with a HR detail. By strictly taking this assumption, and therefore exploiting only one in-situ measurement, the results are still affected by wind and gravitational redistribution that influence the AWS observations. This in turn may perform a complete sensitivity analysis of the method. This has been partially covered by other works (e.g., Slater et al., 2013b; Ismail et al., 2023). Here, we present a simplified sensitivity analysis on the parameters that play a role in the proposed approach. For the sake of clarity, we investigate how the most important parameters affect the final SWE results that are biased by wrong state identification. Moreover, in some remote areas automatic measurements can be completely missing. Hence, there is the need reconstruction by considering the pixel where the station Volcanic Knob provides continuous SWE measurements in the Sierra Nevada catchment. These parameters are i) the DD factor a , ii) the SWE threshold SWE_{min} used to identify the *accumulation* state at HR as done for the *ablation* state using the SAR information. A possible solution is to spatialize the AWS information considering for example elevation bands where the hypothesis of a constant state is more reliable (i.e., a similar concept as the hydrological response unit). Nonetheless, this is a challenging task that requires a well distributed AWS network or to couple our approach with a physically based model able to spatialize correctly the AWS information. Even if the modularity of states, iii) the time of snow disappearance (t_{SD}), iv) the time of snow appearance (t_{SA}), and v) the time of the runoff onset detected by S1 (t_{RO}). We vary each of these parameters separately, keeping the others constant and equal to the optimal case (see Table 4). The test is carried out for the 2018/19 season. Although this analysis is not exhaustive, it gives an overview of the most important sources of error.

In Fig. 12a a varies from 3 to 6 by steps of 0.2 $\text{mm}^\circ\text{C}^{-1}\text{d}^{-1}$. It is possible to notice that the error increases linearly when a moves away from the optimal value, that is 4.5 $\text{mm}^\circ\text{C}^{-1}\text{d}^{-1}$, as set for the SWE reconstruction.

In Fig. 12b the SWE threshold varies from 0 to 20 by steps of 1 mm. As expected, the higher the threshold, the greater the error. Indeed, for thresholds that are too large, the proposed approach allows the separation of the different steps that can be easily interchanged with other possible solutions, this is out of the scope of this paper method does not detect *accumulation* states. A snow threshold of 2 mm, as used in this work, is acceptable.

Table 4. Optimal parameters values for the pixel with the Volcanic Knob station.

<u>Parameter</u>	<u>Unit</u>	<u>Value</u>
<u>a</u>	<u>$\text{mm}^\circ\text{C}^{-1}\text{d}^{-1}$</u>	<u>4.8</u>
<u>SWE_{min}</u>	<u>mm</u>	<u>2</u>
<u>t_{SD}</u>	<u>d</u>	<u>2019/06/27</u>
<u>t_{SA}</u>	<u>d</u>	<u>2018/11/22</u>
<u>t_{RO}</u>	<u>d</u>	<u>2019/04/22</u>

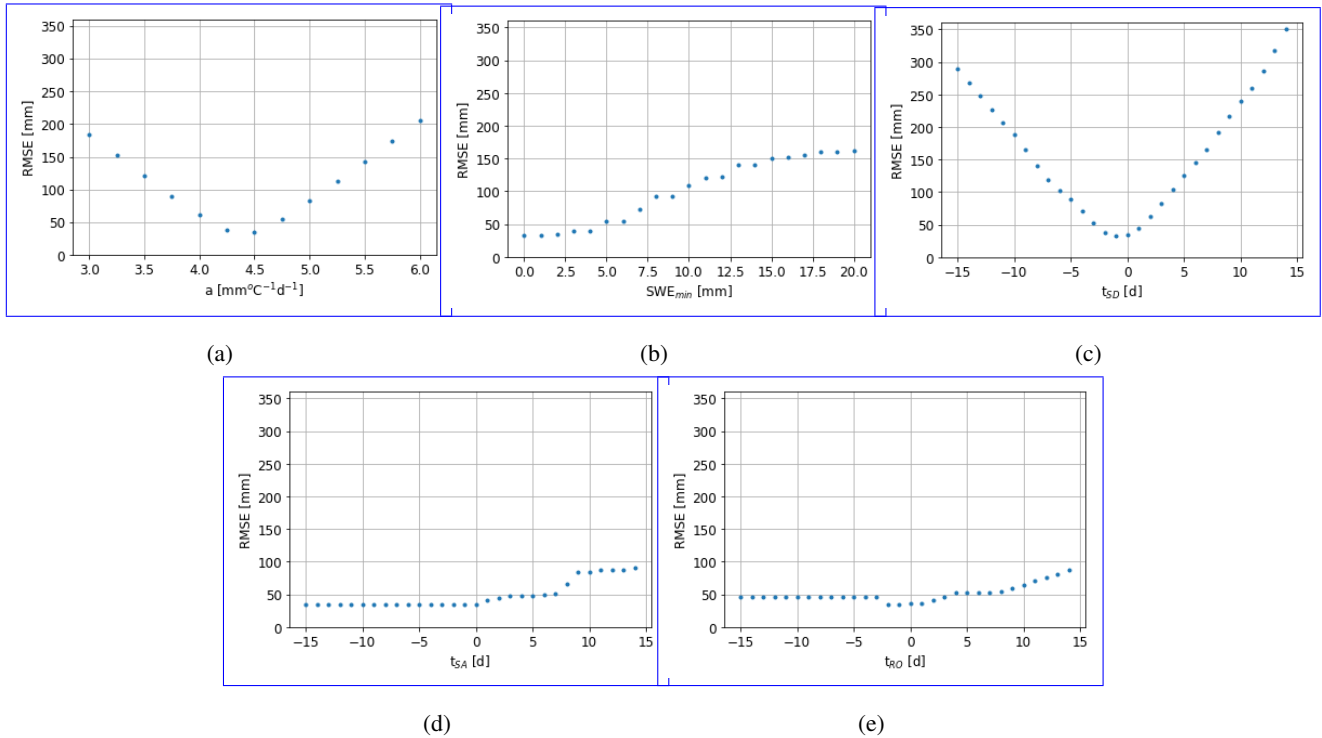


Figure 12. Sensitivity analysis on: a) the DD factor (a), b) the SWE threshold (SWE_{min}), c) the time of snow disappearance (t_{SD}), d) the time of snow appearance (t_{SA}), and e) the time of the runoff onset detected by S1 (t_{RO}). One parameter is varied while the others are kept constant and equal to the optimal value as reported in Table 4.

700 ~~Another possible solution is to exploit once again the information provide by the satellite missions~~In Fig. 12c t_{SD} varies
in a range of ± 15 days w.r.t. the optimal day. Both underestimating and overestimating t_{SD} introduces important errors in
the reconstruction. Indeed, ~~the use of satellite information collected over larger and remote areas represents an interesting~~
enhancement of the proposed method. The prediction of the catchment state could be provided for example by satellite
information about SCA variations that are connected to SWE changes. Especially at the beginning of the season, an important
705 snowfall is well represented by a strong increment in terms of SCA. However, there are some ambiguities that need to be

solved. For example, when observing constant SCA or when SCA is 100% we cannot determine the state of the catchment. In this sense, the size of the catchment plays an important role that need to be further investigated. As interesting alternative we also mention the use of SAR data. In this work, we exploited S1 to detect the snowpack melting. However, the signal seems to be also sensitive to the presence of fresh snow, showing an increase of the backscattering in correspondence of a snowfall (e.g., Lievens et al., 2022; Tsang et al., 2021). The poor temporal resolution represents however a strong limitation for a practical application at the end of the melting season the temperature is high and consequently the potential melting. A difference of ± 5 days (which corresponds to the repetition time of S2) already introduces an RMSE of approximately 50 mm.

In Fig. 12d t_{SA} varies in a range of ± 15 days w.r.t. the optimal day. The shift of t_{SA} does not strongly affect the RMSE as t_{SD} does. For negative shifts, the RMSE is constant since no SWE is added to the reconstruction. Indeed, for these days, we find that the coefficient k (see Eq. 4) is 0 since it is calculated from the AWSs. In other words, it means that the accumulation is not really happening before at least one station detects an increase in SWE. This might introduce an error if some pixels are in accumulation before the station reports it, but it does not affect the maximum amount of SWE for those pixels, which is determined only by the days in ablation.

In Fig. 12e t_{RO} varies in a range of ± 15 days w.r.t. the optimal day. Furthermore, the shift of t_{RO} does not strongly affect the RMSE as does t_{SD} . The RMSE for negative shifts remains constant after a certain point, since for those days Eq. 1 returns 0 potential melting due to negative temperatures. This means that anticipating the melting phase is less critical than postponing it, since the temperatures and consequently the potential melting are lower.

In general, we can summarize that changes in a and t_{SD} are expected to strongly affect the results. The DD factor a cannot be considered a constant parameter and has to vary in space and time to minimize the SWE reconstruction error, as pointed out by many researchers (e.g., Ismail et al., 2023). On the other hand, given the high temperature and potential melting values at the end of the ablation, an incorrect estimate of t_{SD} can significantly impact the reconstruction of the SWE peak, resulting in either an overestimation or underestimation. Therefore, the introduction of an accurate daily HR time series can greatly benefit the SWE reconstruction.

5.2 Error in the SCA derivation and regularization

It is worth discussing here the SCA regularization more in detail. In Fig Figs. 13 and 14 we show the SCA before and after the regularization for the South Fork SFSJR and Schnals catchments, respectively. As explained in Sec. 5.2, due to the snow cover detection algorithms employed in the proposed method 2.2, the raw reconstructed SCA presents two issues: i) strong decreasing peaks in correspondence of the to HR acquisitions at the beginning of the season that indicate, indicating an underestimation of SCA in forested areas, and ii) small increasing peaks in correspondence of the to HR acquisitions in the late melting phase that indicate, indicating the presence of snow patches that are missed by LR sensors. The not visible in LR images. In contrast, the regularized SCA is instead more stable more stable, and the spurious oscillations, present especially during the most cold coldest winter period, are corrected. The effectiveness of the correction is also visible by looking at a corrected when looking at the regularized image. Fig. 15 represents a common situation when foggy where atmospherically corrupted and mixed pixels are classified erroneously. The proposed correction improves the snow detections snow detection, especially in these complicate

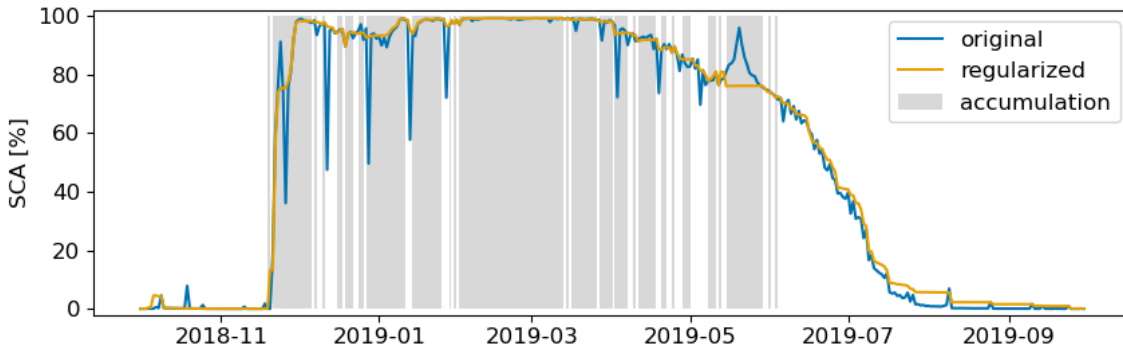
740 complicated cases.

An evident case where an overestimation of the SCA is introduced is in the season 2020/21 in May/June for the South Fork catchment (see Fig. 13c). This error is due to the fact that the AWS do not indicate an *accumulation* in correspondence of the peaks that happen in the late melting phase. Hence, the label is corrected according to the majority rule in *ablation* in the case of an old snowfall (see Sec. 2.2 and Algorithm 1). Many pixels are considered as TP, leading to the propagation of the *snow* pixels backward and the consequent overestimation of SCA. This in turn leads to an overestimation of the SWE as shown in the results (see Sec. 4.1). On the other hand, an underestimation of the SCA is introduced for example underestimation of SCA is observed in May 2019 for the South Fork SFSJR catchment (see Fig. 13a). By an accurate inspection A careful examination of the conditions that lead led to the flattening of the SCA during the late snowfall , it has been showed reveals that the stations indicate a long period as *accumulation* , i.e., from 16th until the 29th of May, while (from 16 to 29 May), whereas the peak starts decreasing in the original SCA time-series starting from the 21st of May. According to the majority from 21 May. By applying the rule for a recent snowfall , the pixels are marked as FP. In fact, the most frequent label is (see Sec. 2.2 and Algorithm 1), the majority of the pixels are labeled as snow-free. In other words, the peak lasts only a few days, so the label snow-free snow since they are snow-free for sure from t onward and this implies the replacement with does not persist for a long time. This implies a replacement with snow snow-free backward until the day of the last ablation. It is possible that the AWS AWSs present some sensor errors, but this could also be the case of a mixed state inside the catchment. In other words, the AWS reveal a snowfall AWSs detect snowfall, but this is most likely happening occurring at high elevations, while the SCA is decreasing due to an ongoing melting decreases due to ongoing melting or rain-on-snow, especially in the lower elevation belts of the catchment (SCA. Indeed, the SCA decrease from $\sim 100\%$ to $\sim 80\%$ means that low quotes are getting snow-free). It may be possible that at low quotes it rained while at higher quotes the AWS correctly detect a snowfall elevations become snow-free. However, we expect that such an ephemeral snowfall is not affecting ephemeral snowfall does not significantly affect the total amount of SWE, as we have seen in the shown in Sec. 4.1. As future perspective, it is worth noting that the availability of more HR images (e.g., Landsat-9) will help to mitigate the errors in the daily SCAreconstruction

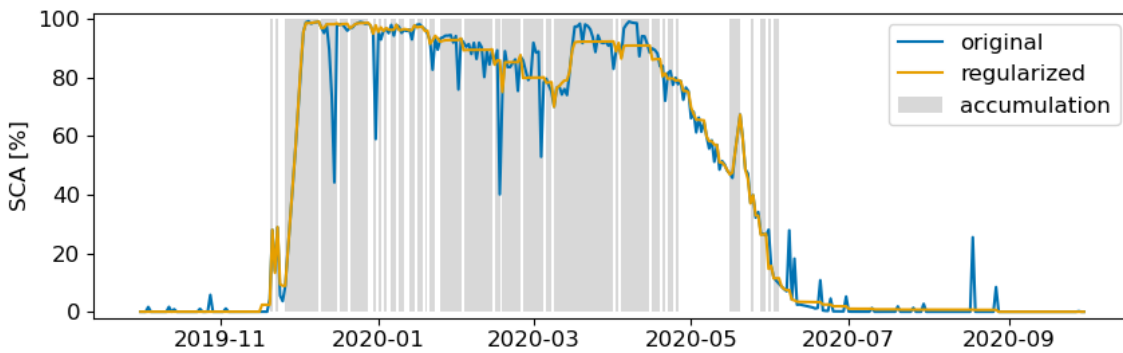
On the other hand, an evident case where an overestimation of the SCA is introduced is in the season 2020/21 in May/June for the SFSJR (see Fig. 13c). This overestimation is caused by the fact that the AWSs do not indicate an accumulation in correspondence with the peaks that occur in the late melting phase. Therefore, the label is corrected according to the majority rule in ablation in the case of old snowfall. Most of the pixels were snow in previous HR acquisitions, leading to the propagation of the class backward and the consequent overestimation of the SCA. This could be a reason for an overestimation of the SWE as shown in the results (see Sec. 4.1).

770 **5.3 Error in the SWE reconstruction**

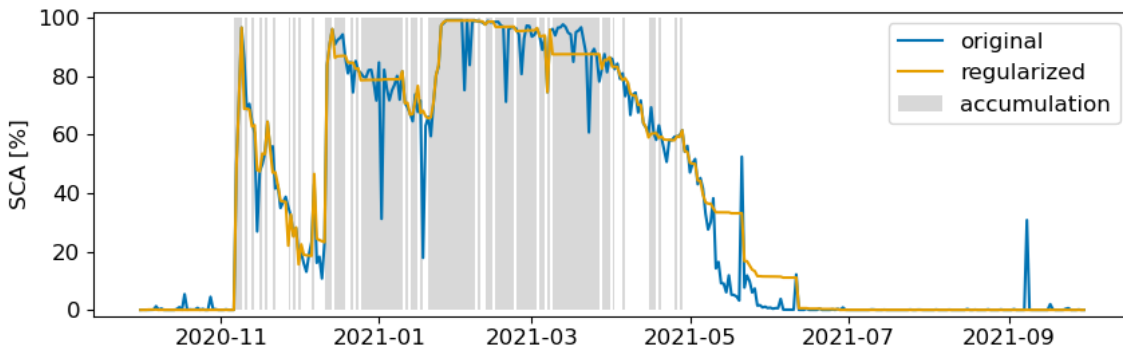
In Sec. 4 we have presented the results of the proposed method. We have shown the differences that arise when comparing the results of our method with a spatialized product (ASO). We would like to discuss here the sources of error and the major weaknesses of the proposed method. The potential source of errors are represented by i) the temperature data, that in turn affects



(a)

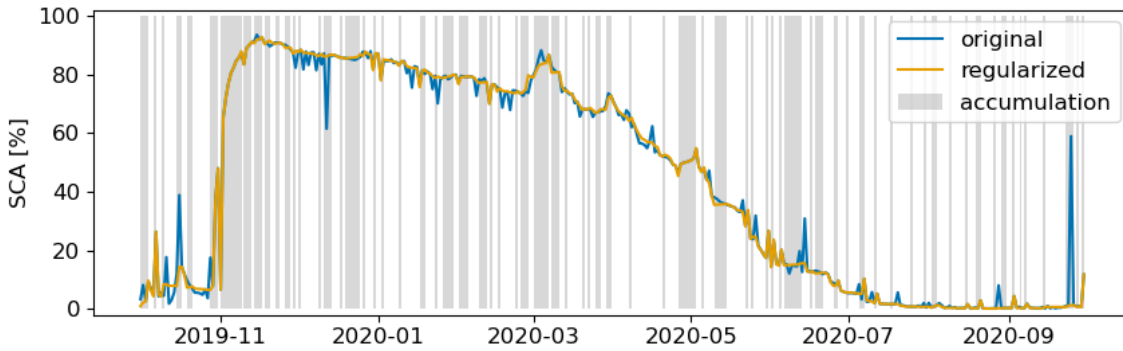


(b)

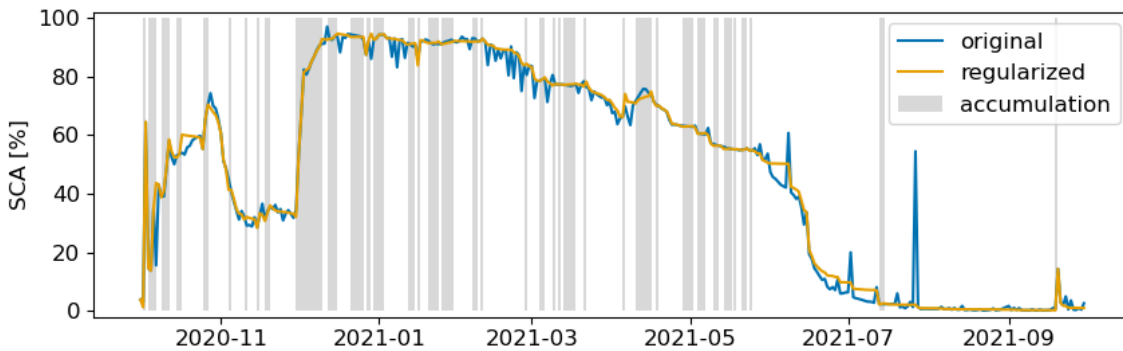


(c)

Figure 13. Trends of the SCA time-series in the South Fork catchment SFSJR for the hydrological seasons a) 2018/19, b) 2019/20 and c) 2020/21. Original input version (in blue) and corrected regularized version (in orange) after the application of the proposed regularization. The gray background color corresponds to an accumulation state.



(a)



(b)

Figure 14. Trends of the SCA time-series in the Schnals catchment for the hydrological seasons a) 2019/20 and b) 2020/21. Original input version (in blue) and corrected regularized version (in orange) after the application of the proposed post-filter. The gray background color corresponds to an accumulation state.

775 the DD model, and ii) the wrong identification of t_{SA} and t_{SD} , that depends on the accuracy of both the SCA time-series and the catchment state. Since the input data are subjected to several degrees of preprocessing, it is difficult to carry out a specific sensitivity analysis of the problem. The most important factors are discussed in the work of Slater et al. (2013b). Instead, we perform here a critical analysis for better defining future developments to improve. It is evident that the effectiveness of the SCA regularization is strongly influenced by the reliability of the state identification. At the current state, the main limitation of the proposed method is:

780 The implications of a wrong detection of t_{SD} are much more important than the wrong identification of t_{SA} . At the end of the ablation period, M is high and therefore the total SWE for a pixel, which is given by the potential melting integrated over time for days in ablation, can be strongly altered by introducing either an overestimation or an underestimation, depending on

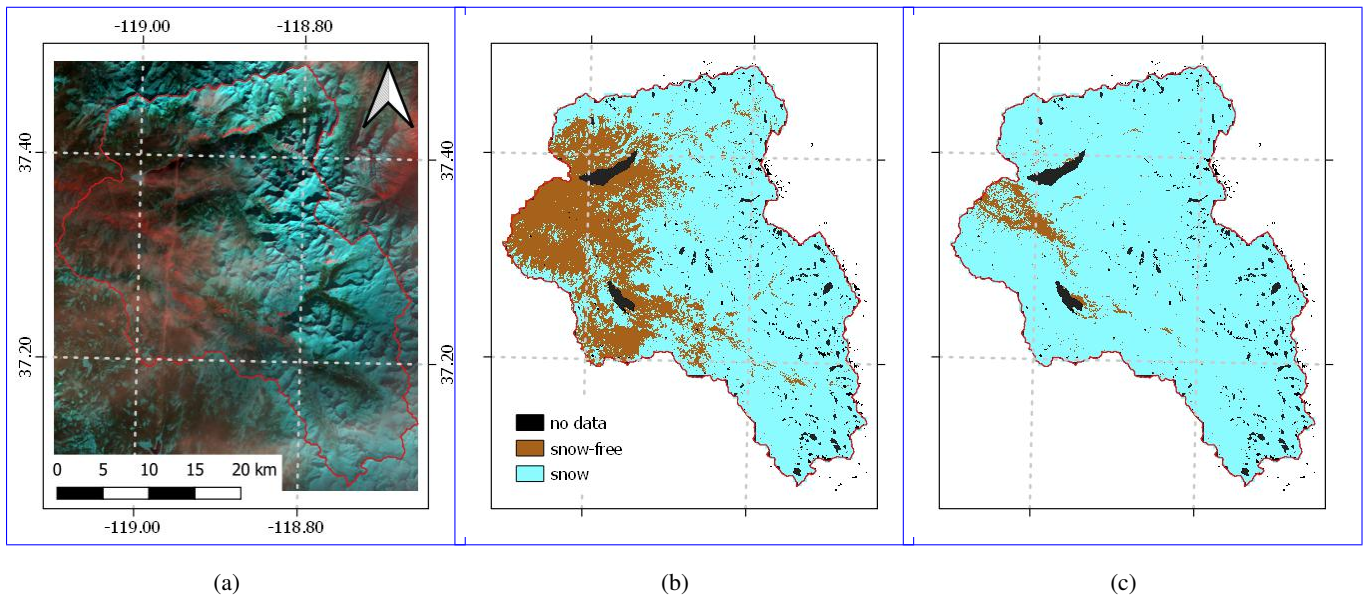


Figure 15. Example of a regularized snow map on ~~the date-12 /01/January~~ 2020 for the ~~South Fork catchment~~SFSJR: a) false-color composition (R:SWIR,G:NIR,B:RED), b) ~~input-original~~ snow cover map, and c) regularized snow cover map.~~Background-image ©Google Maps 2022.~~

785 the case. The error can also be propagated for several days during the melting season. On the contrary, in the period of the year when most consistent snowfalls happen at the beginning of the season, the days in *ablation* are few, temperatures are low, consequently M is negligible (see Eq. 1) and does not change so much from one day to the other.

790 The use of a simple DD-model for computing the potential melting is another source of error. This simple model does not take into account different energy inputs due to either geomorphometrical features or different periods of the year, since we used a constant DD factor. This may be the case of the overestimation of SWE happening during the hydrological season 2020/21 as shown in Sec. 4.1. In fact, this year presents an anticipated melting. Hence, we expect a lower energy input w.r.t. the season when the DD factor has been calibrated. Even though we are aware of the limitations of such a simple model, we did not consider the use of a more complex model, since this is not the focus of this work. An interesting further development is to test the approach with a more sophisticated potential melting estimation. Since the potential melting is calculated separately, this step can be easily replaced.

795 As potential correction of the DD model, we proposed is represented by the accumulation identification which is not provided at a pixel level. Future research should focus on this point and exploit remote sensing observations rather than sparse AWSs information. For example, a possible indicator of an ongoing accumulation is represented by a SCA increase. However, small variations may be due to errors. Furthermore, snowfalls on already snow-covered areas cannot be identified. A possible alternative is represented by the use of S1 for identifying the timing of the melting phase. In fact, it may be that the DD detects high temperatures but the energy is still not sufficient to cause the snowpack melting. Even though we do not

800 expect big differences since temperatures are low in the first phase of the melting and consequently the potential melting is low, the spatialization of temperature may also be affected by possible errors. S1 represents a spatialized way to identify the melting, but it presents as major disadvantage a poor temporal resolution, i.e., few days. As future development, we aim at exploiting S1 and the new HR land surface temperature acquired by the next Sentinel generation as a proxy of the potential melting estimation, thus enlarging the applicability of the proposed method in remote areas.

805 Finally it is worth mentioning that, the uncertainty introduced in the method are also linked to the high spatial heterogeneity of the SWE. It is possible to encounter a very large variability also within a pixel with size of 25 m as shown by the SWE measurements acquired in Schnalstal by Warseher et al. (2021). This results in an intrinsic difficulty to evaluate the output with an appropriate reference data SAR data. Recent works have shown that the backscattering seems to be sensitive to the presence of fresh snow, showing an increase in the backscattering in correspondence with a snowfall (e.g., Tsang et al., 2021; Lievens et al., 2022).
810 However, the poor temporal resolution may strongly affect the *accumulation* rather than the *ablation*, since the snowfall is expected to be a more rapid phenomenon.

6 Conclusions

In this work we presented a novel approach to reconstruct daily HR SWE maps for a mountainous catchment. We started by, we explored the use of multi-source satellite data to reconstruct HR daily SWE time-series at a spatial resolution of
815 25 m. The proposed approach involves the following step: i) determining the state of the catchment, (i.e. if it is subjected to, *accumulation* (increase of SWE), *ablation* (decrease of SWE), or *equilibrium* (constant SWE). The state was identified exploiting both i) using in-situ SWE or SD data, which provide information about the snowfall; and ii) multi-temporal SAR information to decide if the pixel is melting. Moreover, a novel daily HR SCA time-series was used to determine SD/SWE observations and S1 multitemporal backscattering data, ii) identifying the dates of snow appearance and disappearance ;
820 which represents an information with unprecedented spatial and temporal detail. The from a daily HR snow cover time-series derived by fusing high- and low-resolution optical sensors, and iii) estimating the potential melting from in-situ temperature observations using a DD model. We proposed a novel regularization of the SCA time-series was opportunely regularized according to the catchment state. Furthermore, the state was also used as necessary information for the SWE reconstruction that considers the state information. The regularization corrects impossible transitions, i.e. whether, erroneous changes of the pixel class from *snow* to *snow-free* when *accumulation* or *equilibrium* and, vice versa, from *snow-free* to *snow* when *ablation* and
825 *equilibrium*. Finally, the SWE is added or removed. The potential melting was estimated by mean of a simple DD model after having spatialized in-situ temperature observations. The SWE was reconstructed for the entire snow season without the need of precipitation data as input. The results obtained for two different test sites, i.e., the South Fork catchment and from the reconstruction according to the state, with the amount determined by the potential melting calculated using the DD model.

830 The proposed novel state concept is utilized throughout the different steps of the method, resulting in a SWE reconstruction that incorporates the accumulation phase and potential late snowfalls. Furthermore, spatialized precipitation data, which can be unreliable on complex terrains, is not required as the method redistributes the amount of melting by leveraging state information

rather than quantifying precipitation input. The state also enables the implementation of a new regularization of the SCA time-series. Additionally, the use of a daily HR SCA time-series in combination with melting phase information from SAR data is introduced as a further innovation.

The method was tested in two mountainous catchments: i) the SFSJR, located in the Sierra Nevada - California (USA), and ii) the Schnals catchment, located in the Alps - South Tyrol (Italy). The results obtained demonstrated the effectiveness of the proposed approach to estimate the in estimating HR SWE. For the first catchment, the results were evaluated against the ASO SWE product-ASO SWE at 50 m, showing an average bias of -40 mm-22 mm, an RMSE of 212 mm, and a correlation of 0.74. When evaluated against the daily WUS-SR dataset at 500 m resolution, they showed a bias of -44 mm, an RMSE of 127 mm, and a correlation of 0.66. For the second site, the results were evaluated against manual measurements, showing a bias of 38 mm-5 mm, an RMSE of 191 mm, and a correlation of 0.35. The obtained results were extensively discussed also considering possible hydrological applications of such a productdataset. In this sense, we have seen-showed that the results are very promising ,since they i) are able to well-capture the typical spatial variability of a HR-productan HR map, ii) show spatial patterns that are consistent with the reference-producta reference with comparable spatial resolution, as well as with the geomorphology-topography of the study area, iii) provide a reliable global balance at a catchment scale, and-iv) reproduce the variability of different hydrological seasons, and v) require limited meteorological and ground snow observations.

Finally,we-can-state-thatThe main sources of error are discussed to provide insights into the main advantages and disadvantages of the method that may be of great interest for several hydrological and ecological applications. It was found that the main sources of errors arise from the potential melting calculation and from the time of snow disappearance. To address potential melting errors, we presented a method that incorporates spatialized information from S1 to determine when the snowpack is subject to runoff and prevent false early melting. Secondly, we introduced the use of HR SCA for SWE reconstruction, which is more adequate to sample the variation-of-SWE-SCA variations due to the complex topography of mountainous catchments. Some technological limitations are present (e.g., Technological limitations are still present, such as the necessity of merging LR and HR sensors given the absence of daily optical HR acquisitions, the absence of an appropriate observation to determine the accumulation state pixel-wise, and the scarce temporal resolution of SAR acquisitions).-Even-though-. Although the proposed approach tries-attempts to overcome all these limitations, we expect that further improvements will be-introduced-also-also be introduced by future satellite missions, such as Copernicus LSTM and ROSE-L, which will acquire new important information for SWE retrieval. This will open-opportunities-not-only-to-not-only improve the proposed method but also to-obtain-a-near-real time-predictor-enable the development of near-real-time predictors of SWE for large hydrological and ecological applications.

Code and data availability. The implemented code can be made available upon request to the authors. All the raw input data are freely available as indicated in Sec. 3. The dataset output related to this article will be made available in an open repository after publication or requested directly to the authors.

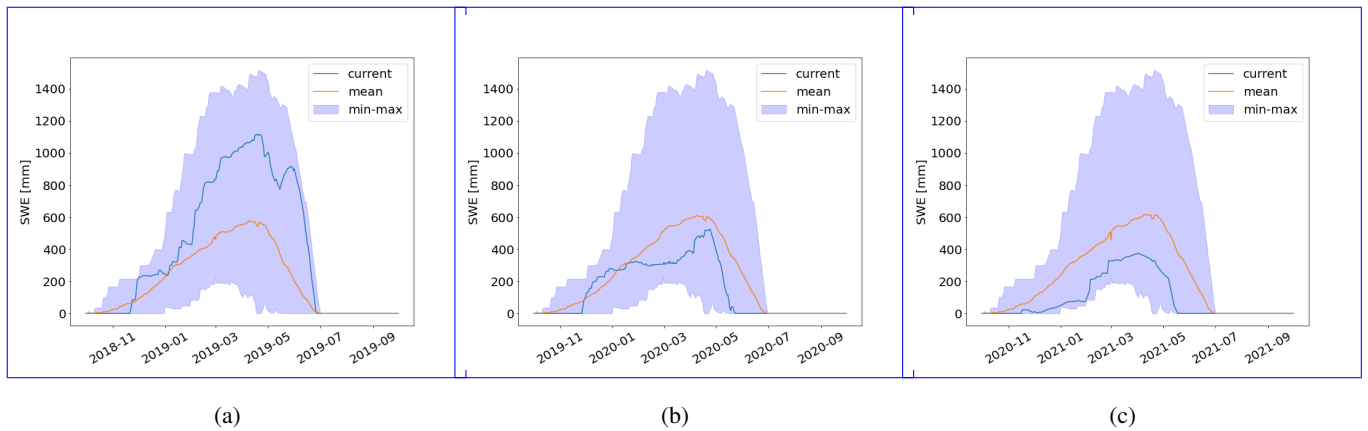


Figure A1. Average SWE (in orange) against the current SWE (in blue) and the range min-max SWE (in violet) at the Volcanic Knob test site for the hydrological seasons a) 2018/19, b) 2019/20 and c) 2020/21. SWE records are available starting from 2000.

Appendix A: In-situ snow measurements

865 ~~The state characterization is done~~ State characterization is performed by observing available SWE or SD in-situ measurements. For the ~~South Fork catchment~~ SFSJR, SWE continuous measurements are available for 7 different sites. As shown in Fig. 3a, only one station is ~~inside within~~ the considered area, i.e., the Volcanic Knob station (VLC). ~~However, we considered also~~ For this station, SWE records are available starting from 2000. This allowed us to perform an analysis of the SWE regime. In the following plots, we show the average SWE for all recorded years, the range of variation, and the current SWE. It is possible to
 870 see that the first season presents high SWE, while the other two seasons are under the average regime, especially the last one. For the SWE reconstruction, we also considered the stations in the surrounding area to smooth out possible sensor errors or redistribution effects.

In the Schnals catchment, SWE continuous records are available only for the location Bella Vista. For this reason, the decision on the ~~catchment~~ state is based on the SD records available for 5 stations (see Fig. 3b). Three stations are ~~inside within~~
 875 the study area and the remaining ~~ones two~~ are very close to the study area (maximum 5 km).

~~Note that for the same catchment, all the stations show a coherent pattern, meaning that we can consider the catchment subjected to the same major weather forcings.~~

~~In Fig. ?? we also report the location of some of the manual SWE observations collected internally by Eurac Research (Institute for Earth Observation) for the Schnals catchment. These few points have been used in Fig. ?? to show some examples of reconstructed SWE trend and its behaviour against the manual measurements. For an overview of the location of all the collected manual observations used to compute the performances of the approach, see Fig. 3b. Overview of the measurements. Background image ©Google Maps 2022.~~

880

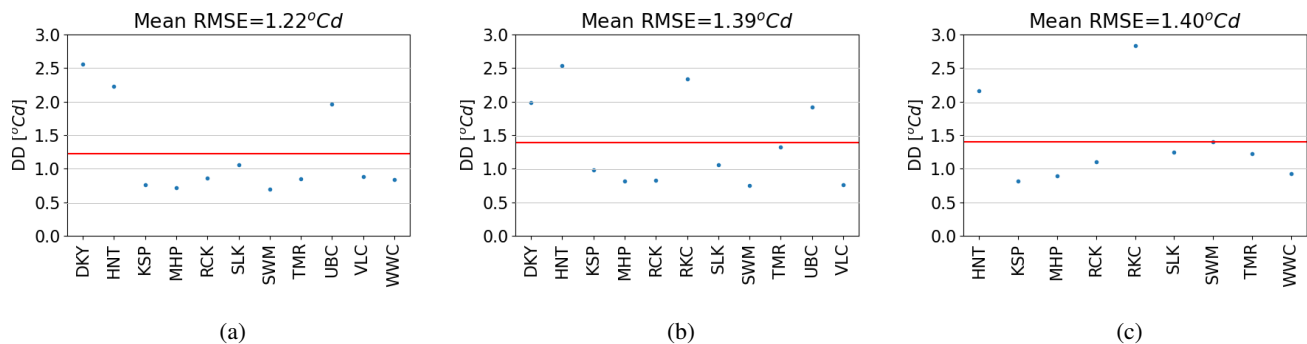


Figure B1. Leave-one-out cross validation results for the ~~South Fork catchment SFSJR~~ for the hydrological seasons a) 2018/19, b) 2019/20 and c) 2020/21.

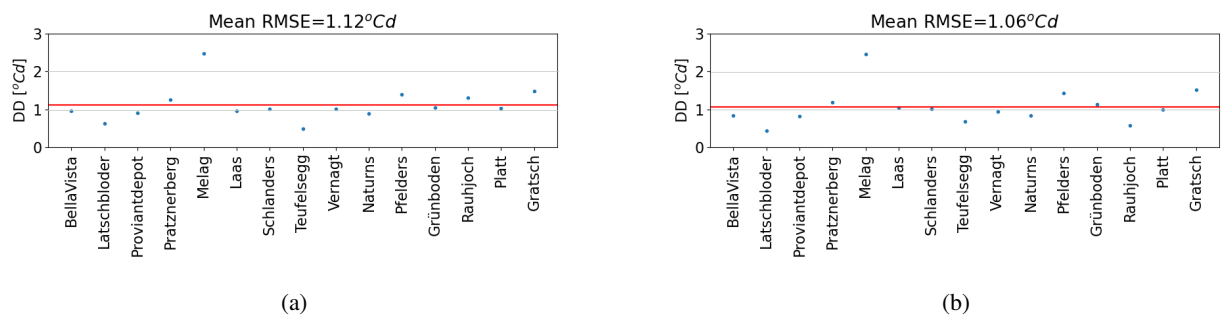


Figure B2. Leave-one-out cross validation results for the Schnals catchment for the hydrological seasons a) 2019/20 and b) 2020/21).

Appendix B: ~~Degree-day~~ Degree-day estimation

The ~~degree-day (DD) is estimated starting from the~~ DD is estimated from available in-situ temperature observations for both
 885 catchments. Regarding ~~the South Fork catchment SFSJ~~, the temperature is available ~~in-at~~ in-at 11 different stations located within
 a radius of ~~around~~ approximately 15 km from the study area (see Fig. 3a). Due to the presence of some gaps in the data, we
 excluded from the computation of the DD the station "RKC" for season 2018/19, "WWC" for 2019/20 and "DKY", "VLC",
 and "UBC" for 2020/21. For the Schnals catchment, the temperature is available in 15 different locations within a maximum
 distance of around 10 km (see Fig. 3b). Once the DD is computed for each station through Eq. 2, the DD is spatially interpolated
 890 with the kriging routine as explained in Sec. 2.3. The goodness of the spatial interpolation is tested through a leave one out
 (LOO) ~~cross-validation~~ cross-validation. The results in terms of root mean square error (RMSE) are reported in Fig. B1 for
~~South Fork SFSJR~~ and in Fig. B2 for Schnals, showing a mean RMSE that never exceeds 1.5°Cd .

Appendix C: SWE results for the South Fork ~~catchment of the San Joaquin River~~

895 Fig. C1 shows the SWE maps derived with the proposed method, the ASO reference ~~product and maps~~, the bias calculated as ~~the~~ difference between the proposed and the reference maps ~~and the dispersion graphs for the 12 analyzed dates over three hydrological seasons (2018-2021) for the SFSJR. The maps have a spatial resolution of 50 m. The scatterplots suggest a dispersion, even though most of the points are generally concentrated on the diagonal.~~

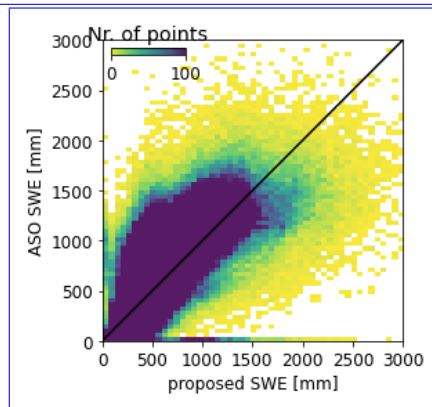
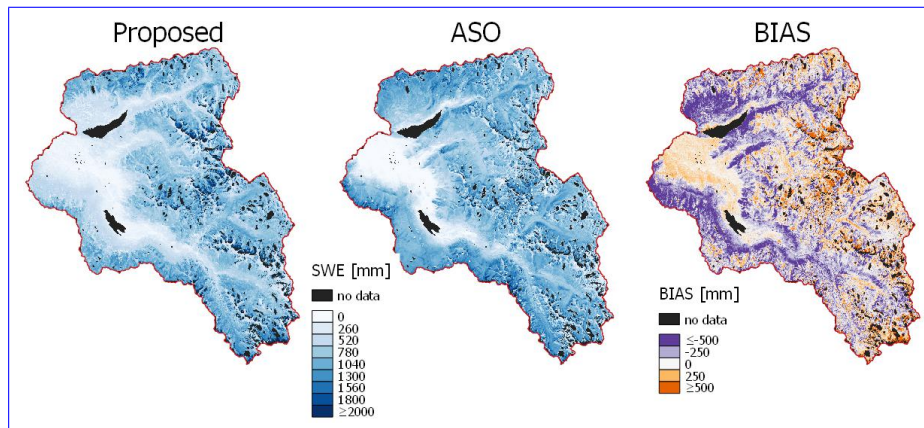
900 Similarly, Fig. C2 shows the SWE maps derived with the proposed method, the ASO SWE maps, the WUS-SR SWE maps, and the dispersion graphs between the proposed and the WUS-SR SWE for the same 12 analyzed dates over three hydrological seasons (2018-2021) for the SFSJR. The maps have a spatial resolution of 500 m.

~~Fig. C3 shows the total amount of SWE calculated for different elevation, slope and aspect bands for the 12 dates when also the ASO product is available. We can notice a general good agreement showing that the proposed method is able to represent the typical geomorphological variability of the snow processes.~~

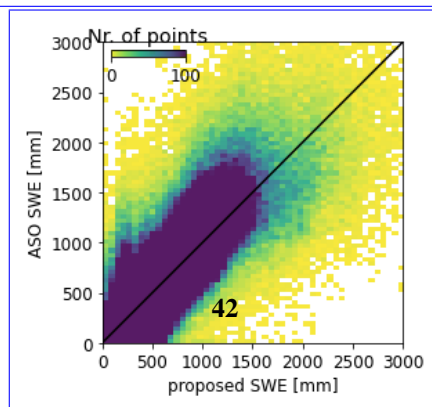
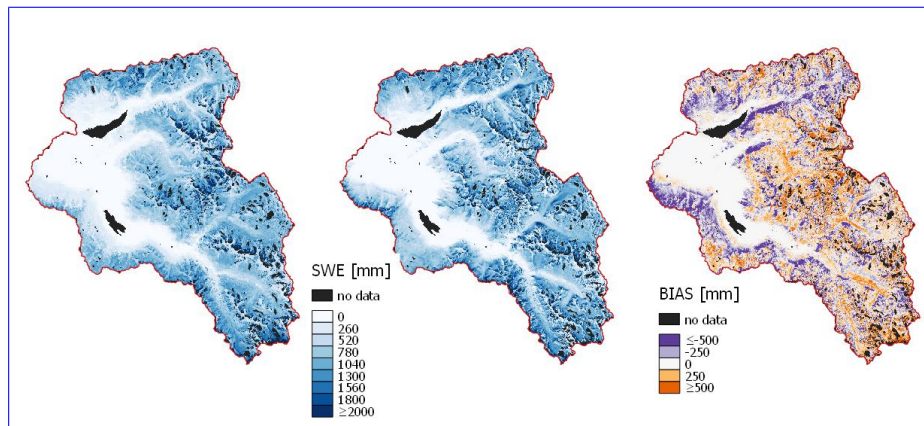
905 ~~Fig. ?? shows the boxplots relative to the total amount of~~ Fig. C3 shows the mean SWE calculated for different elevation, slope and aspect bands for the 12 dates when also the ASO ~~product reference~~ is available. ~~We remind that a boxplot represents the Interquartile Range (IQR) and is composed by the median (orange line), the first quartile Q1 (or 25th percentile) and the third quartile Q3 (or 75th percentile). The whiskers show the "minimum" ($Q1 - 1.5 * IQR$) and the "maximum" ($Q3 + 1.5 * IQR$). In this representation we omit the outliers~~ The analysis is carried out for the proposed method and ASO only, as the high spatial resolution allows for a better appreciation of the complex topographical variability. We can notice a general good agreement showing that the proposed method is able to represent the typical topographical variability of the snow processes. The two datasets show similar trends when compared for different elevation belts. In general, a tendency of the proposed maps to underestimate SWE for lower elevations can be observed, while overestimating SWE for higher elevations. The slope analysis shows larger differences, especially for some dates (i.e., 9 June 2019 and the three images acquired for year 2020) and when considering steep slopes. The proposed method underestimates SWE w.r.t. ASO. However, we generally expect lower SWE for 915 these steeper slopes that promote gravitational transport. The aspect analysis suggests an underestimation for the north facing slope when comparing our dataset with ASO (except for year 2021).

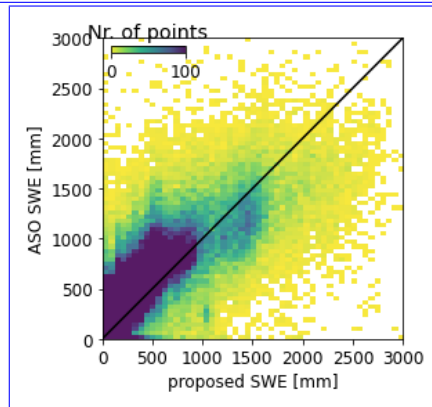
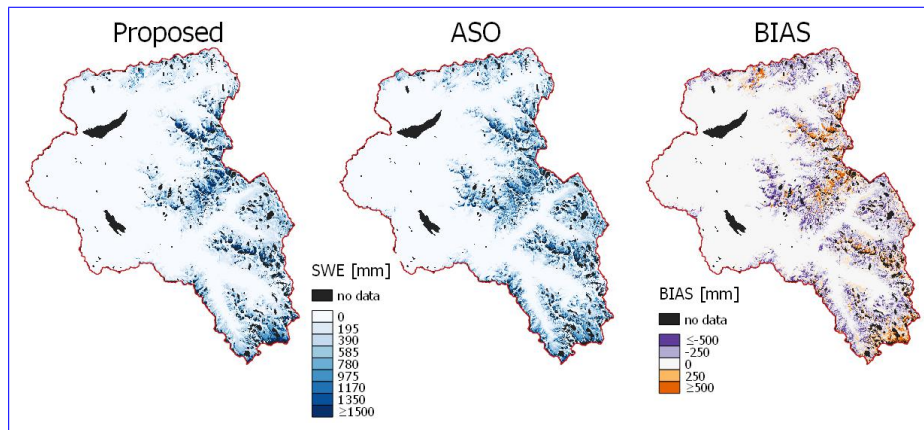
920 In conclusion, we also present in Table C1 the results of the intercomparison between the proposed SWE and the WUS-SR dataset versus ASO for the SFSJR. Bias, RMSE, and correlation are calculated pixel-wise. To this purpose, the proposed and ASO maps were aggregated at a resolution of 500 m. It is possible to notice that the proposed SWE presents a higher bias (an average of -34 mm versus 16 mm), while the RMSE is lower (151 mm versus 193 mm) and the correlation is higher (0.83 versus 0.65).

Author contributions. VP and CM designed the research; VP carried out the experiments and processing; RB provided the HR snow maps from S2; all the authors contributed to the analysis and interpretation of the results; VP wrote the paper based on inputs and feedbacks from all coauthors.

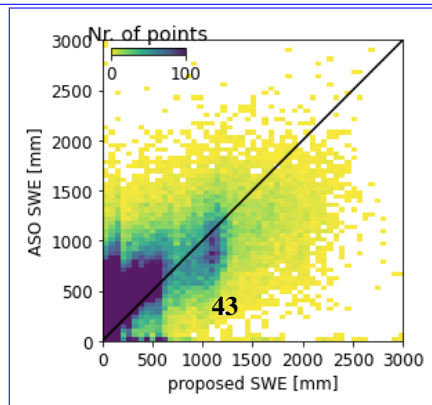
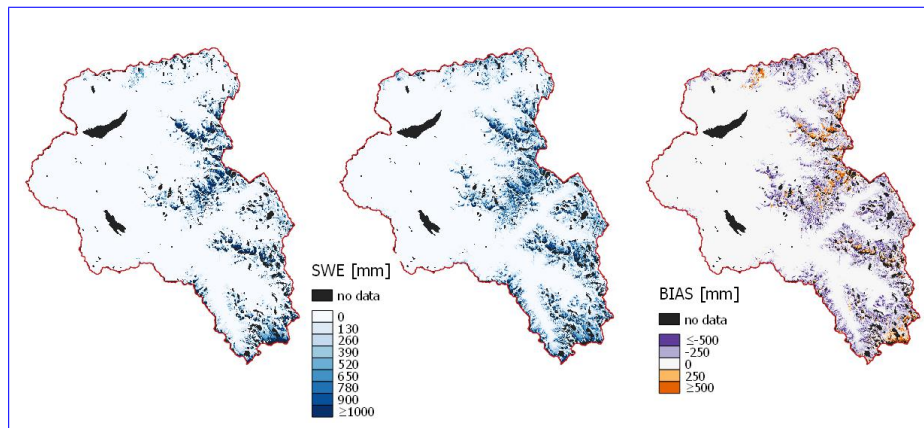


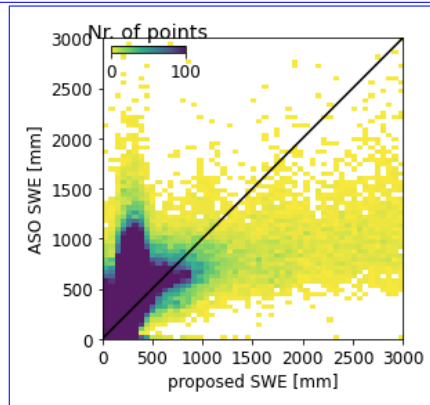
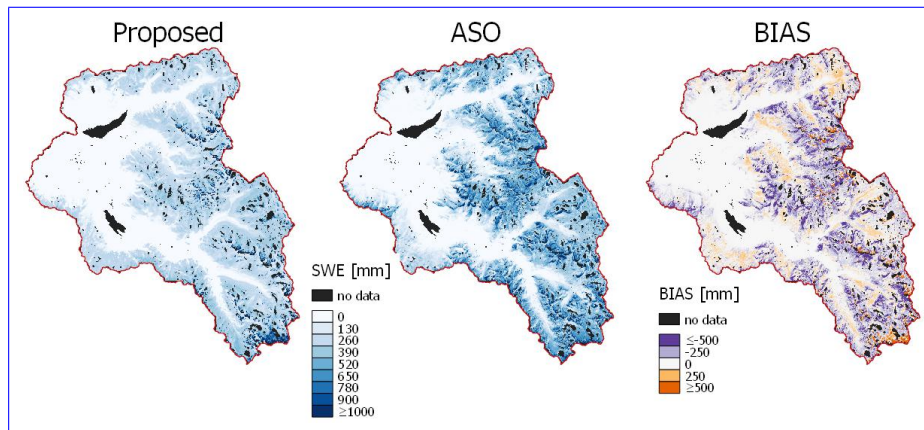
(a) ~~17th~~ 17 March 2019.



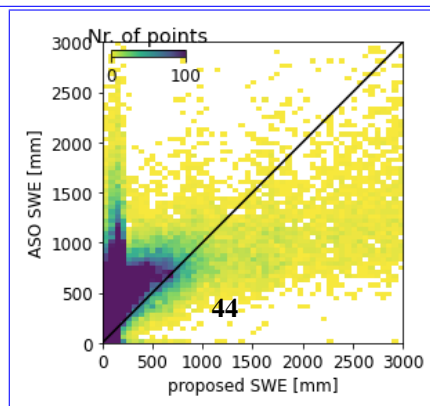
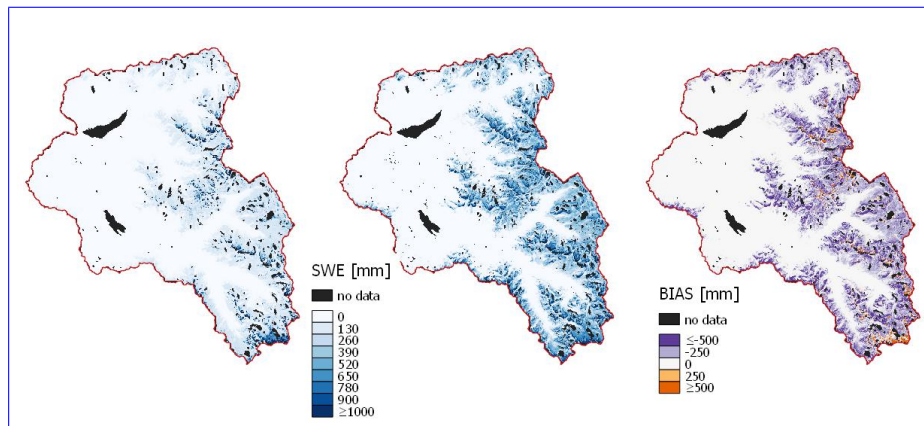


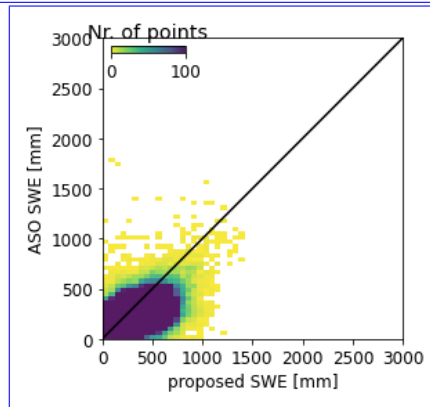
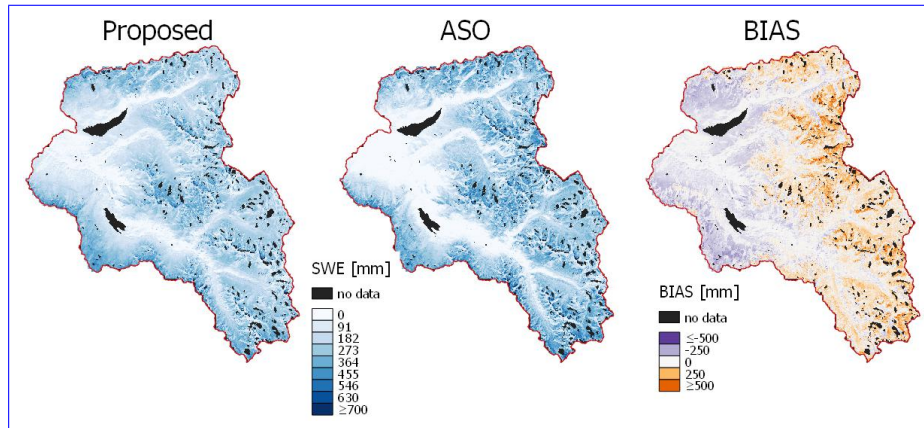
(d) 4th July 2019.



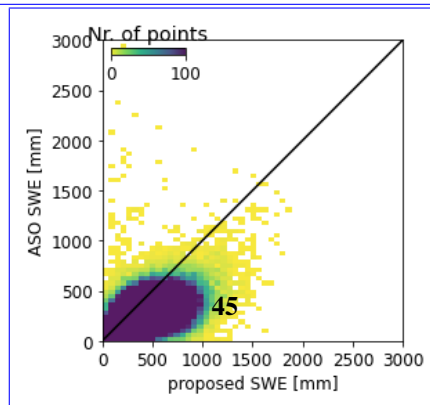
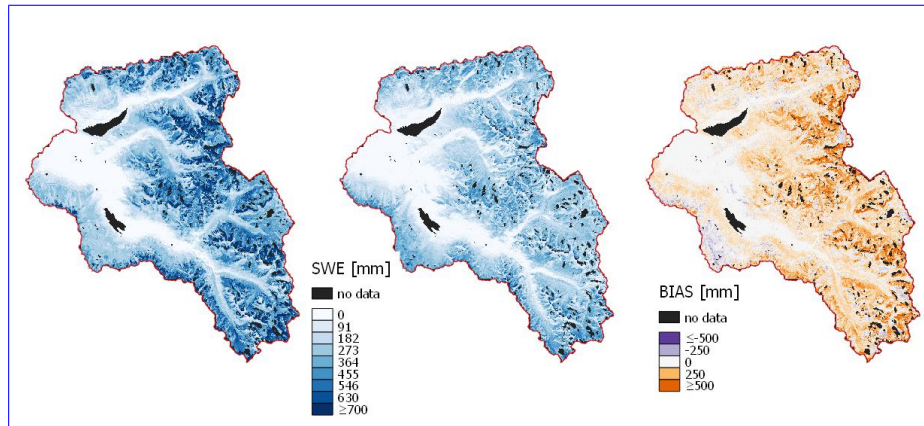


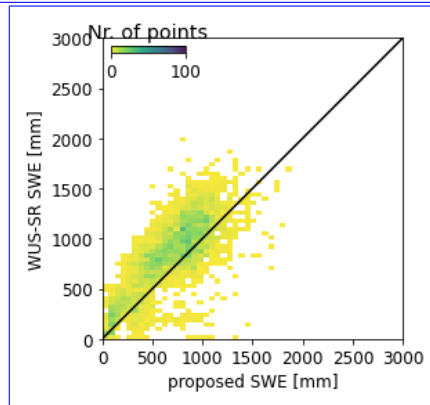
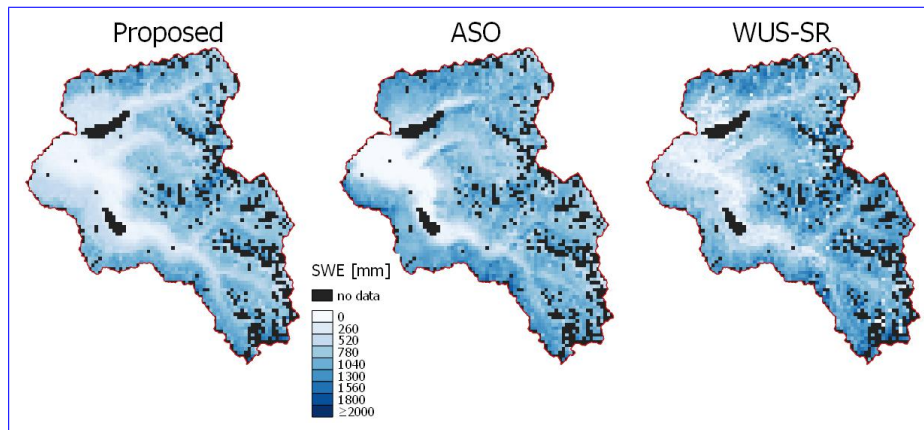
(g) 5th May 2020.



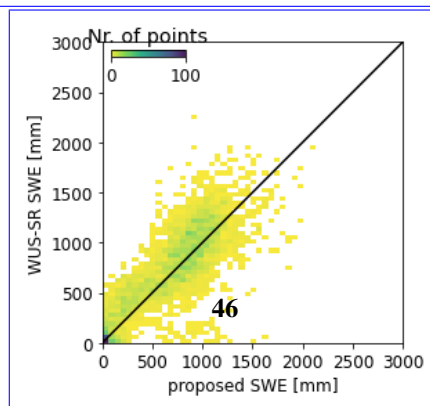
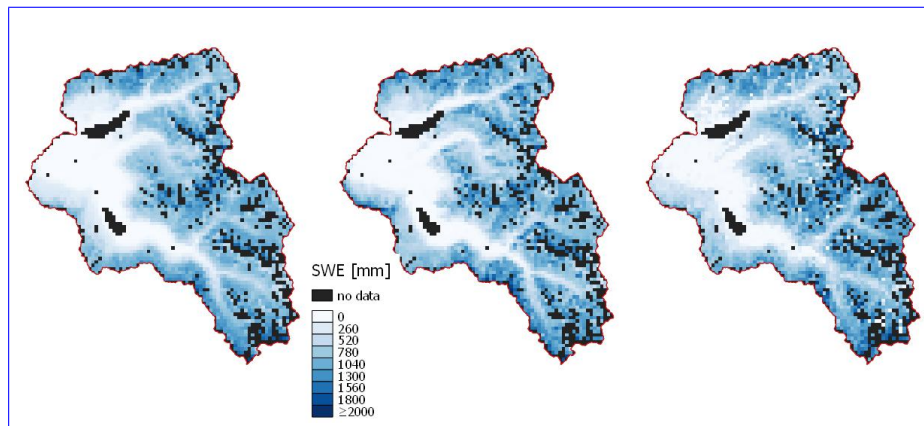


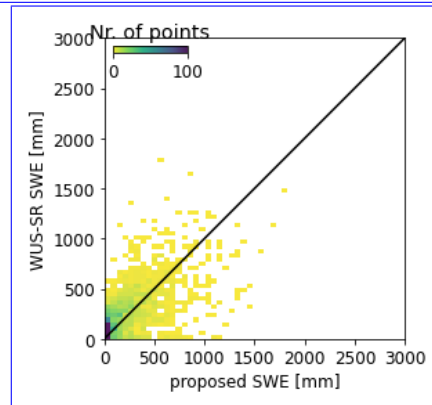
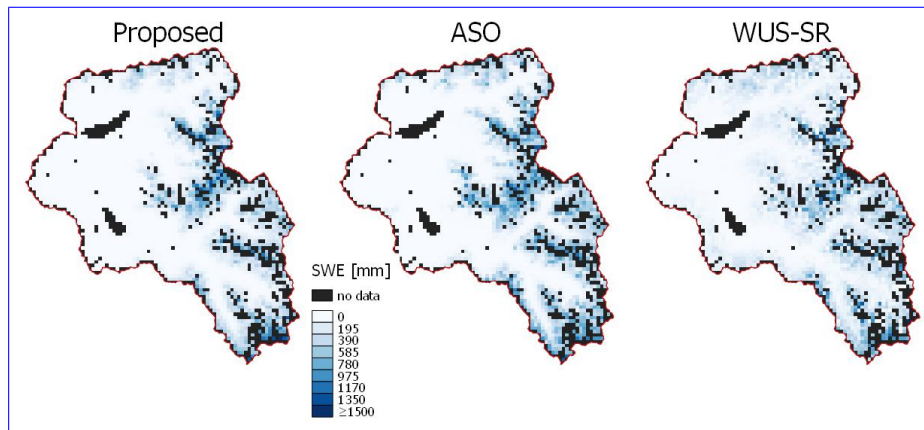
(j) 26th-26 February 2021.



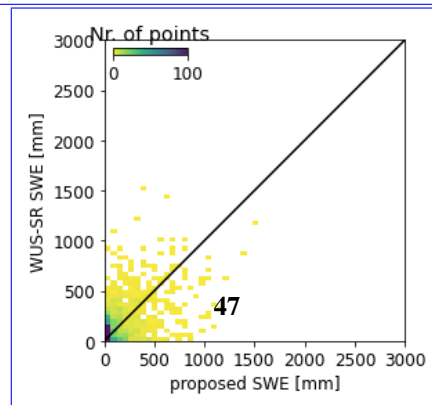
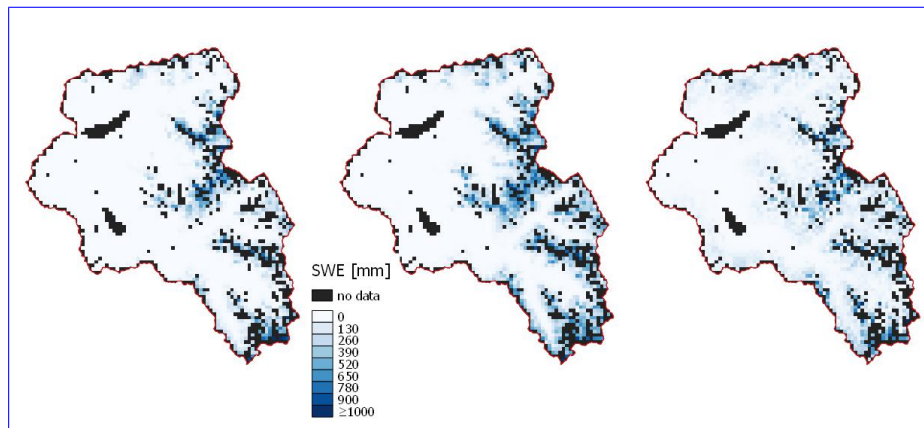


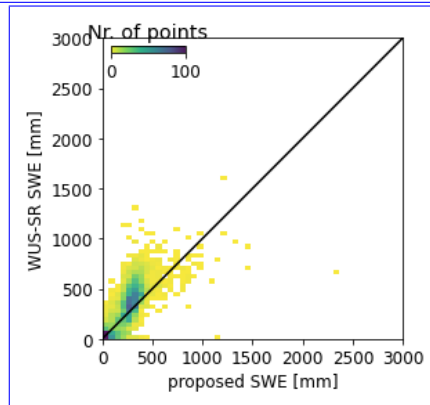
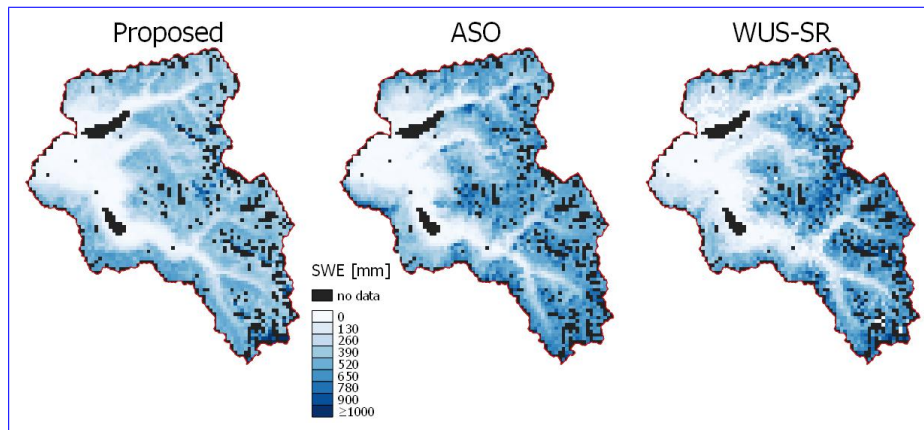
(a) ~~17th~~ 17 March 2019.



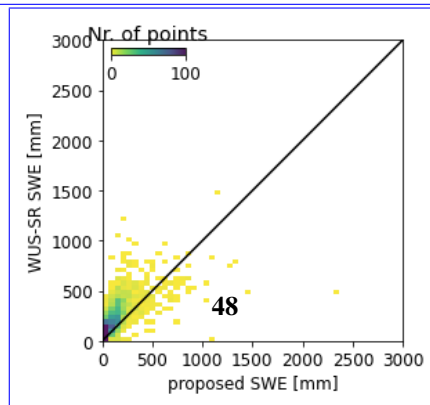
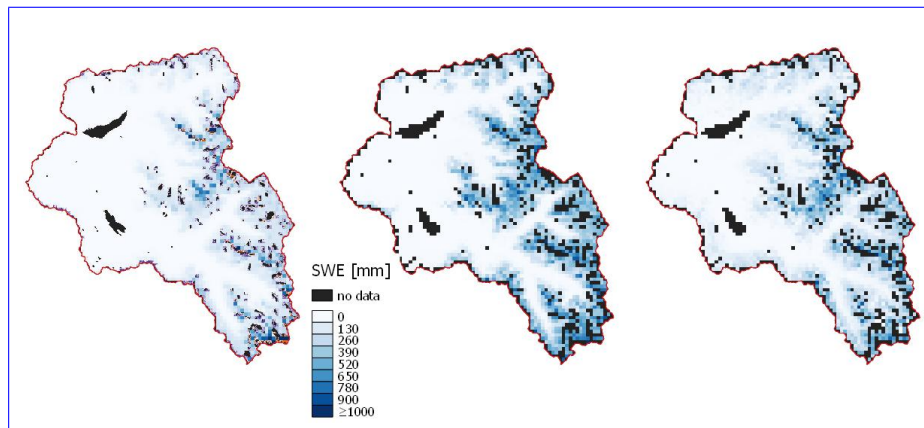


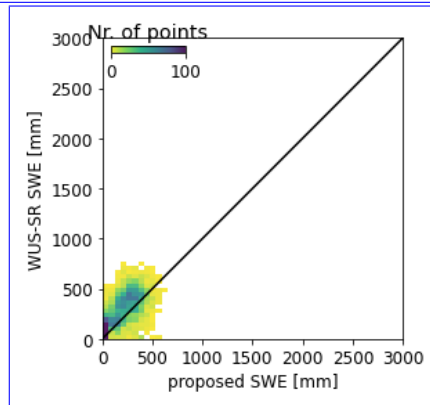
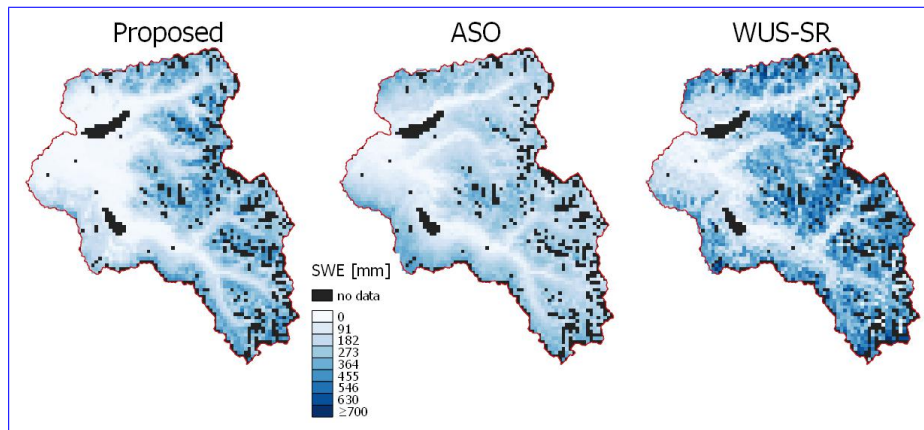
(d) 4th July 2019.



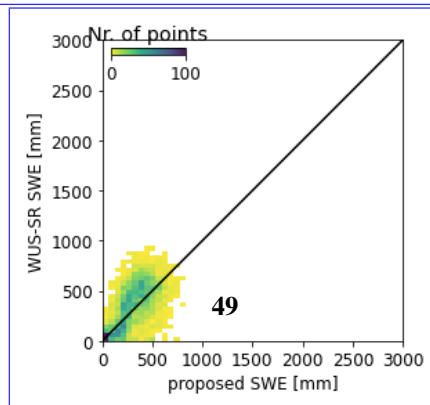
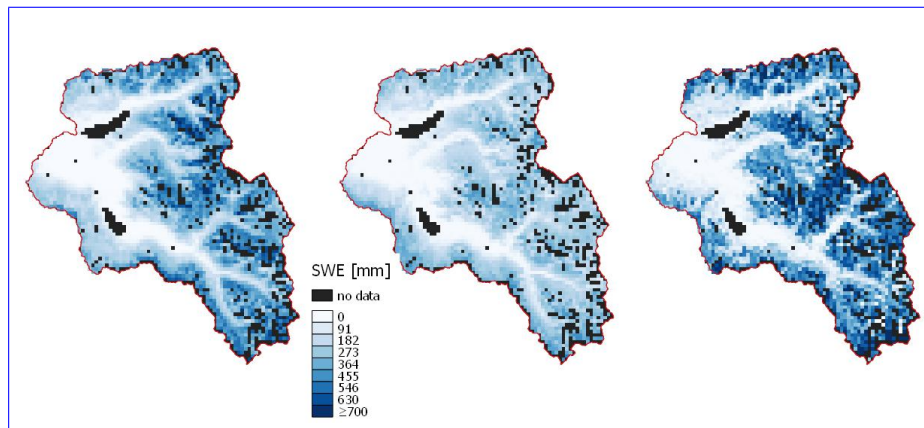


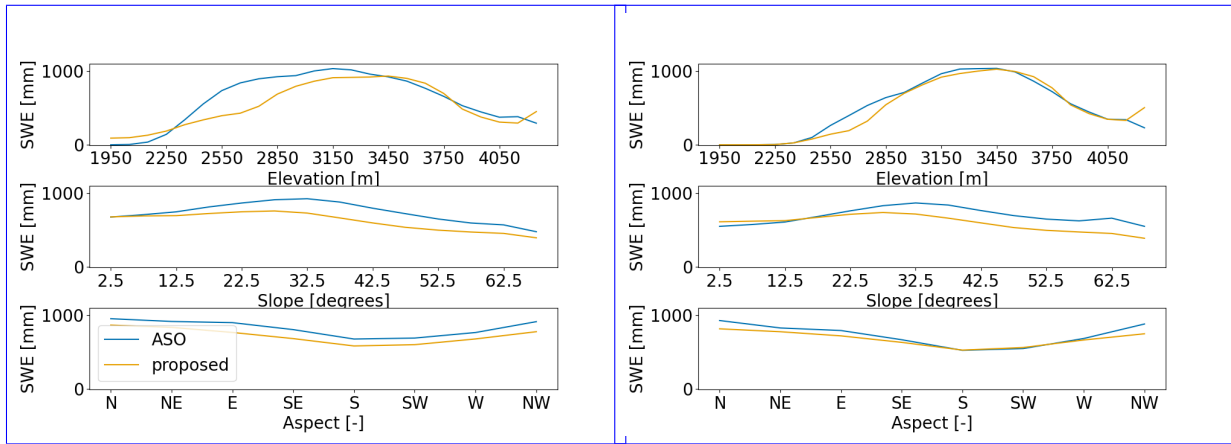
(g) 5th May 2020.





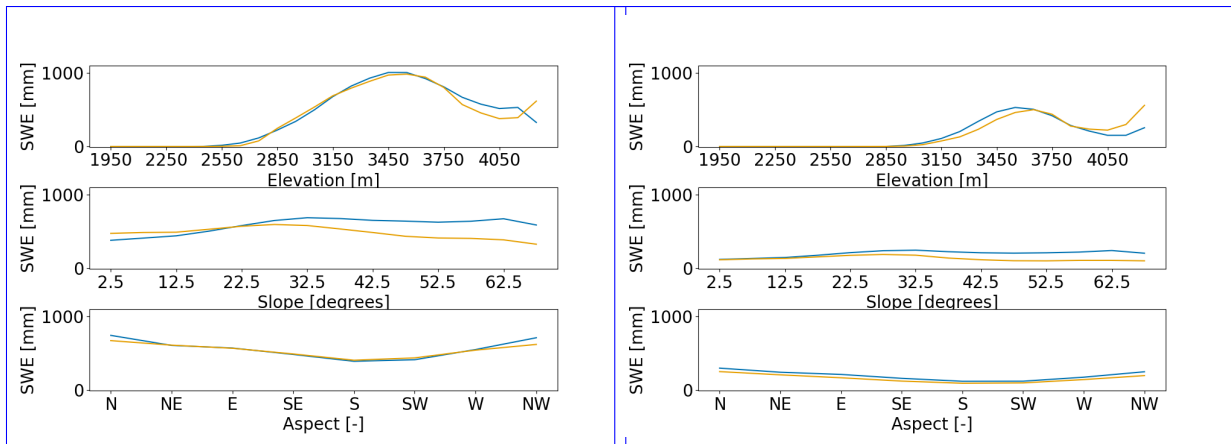
(j) ~~26th-26~~ February 2021.





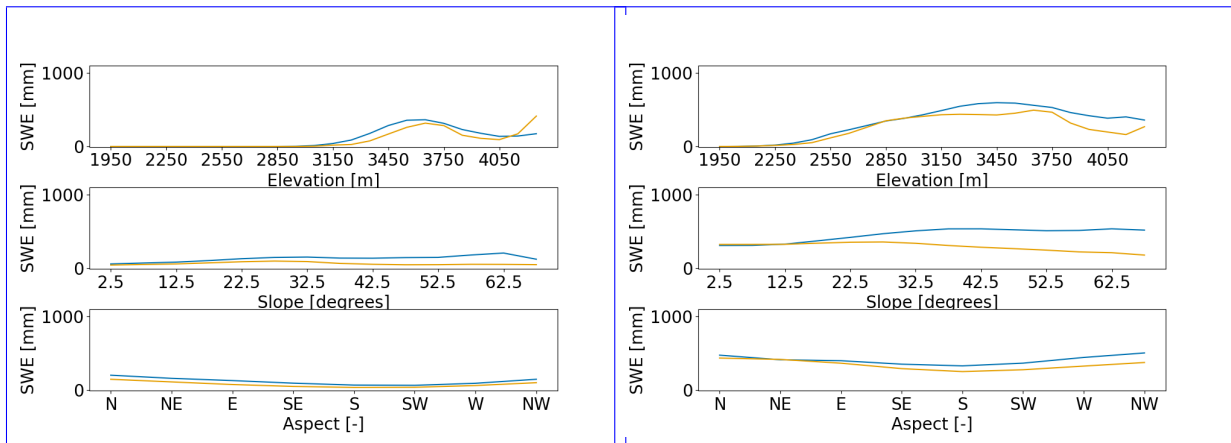
(a) 17th-19 March 2019.

(b) 2nd-4 May 2019.



(c) 9th-9 June 2019.

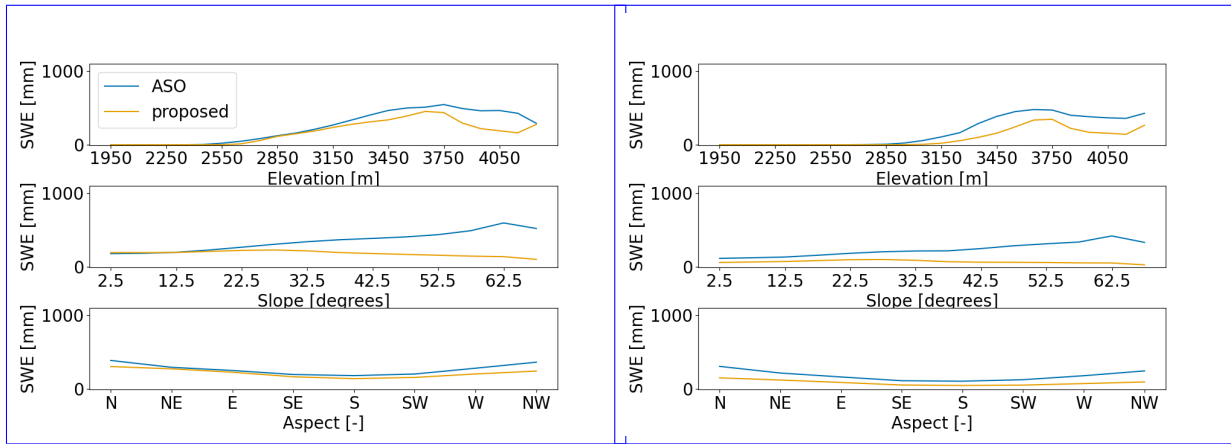
(d) 4th-4 July 2019.



(e) 14th-14 July 2019.

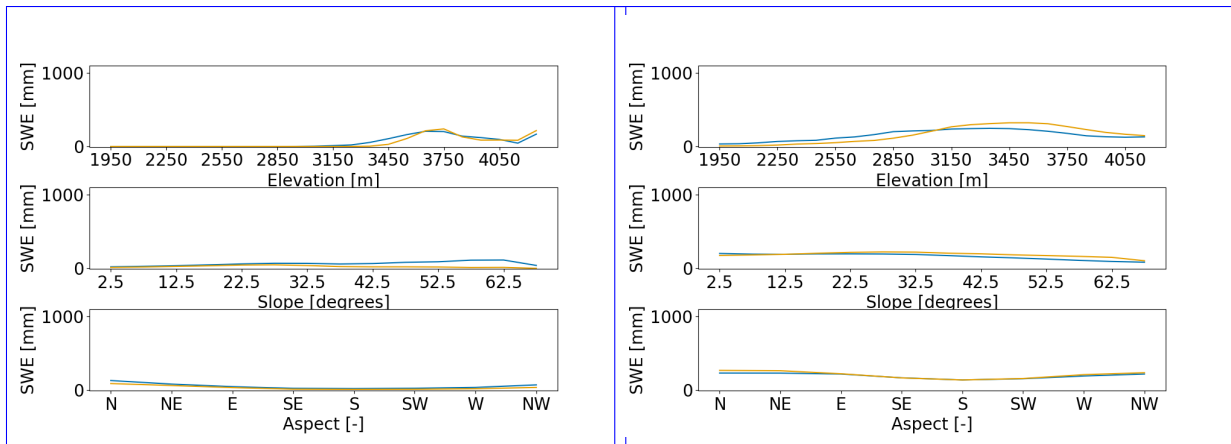
(f) 15th-15 April 2020.

Figure C3. Boxplots of the bias calculated as the Mean SWE generated by the proposed approach minus the ASO product value for each different elevation, slope and aspect belts. The results are represented proposed SWE dataset (in orange) is evaluated against ASO (in blue) for the 12 analyzed dates over the three hydrological seasons (2018-2021) for the South Fork catchment SFSJR.



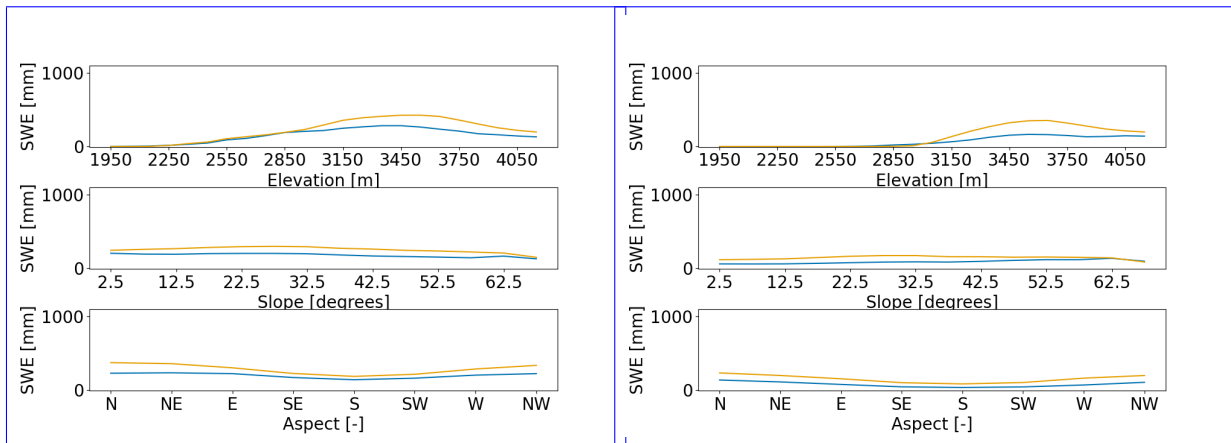
(g) 5th May 2020.

(h) 23th May 2020.



(i) 8th June 2020.

(j) 26th February 2021.



(k) 31st March 2021.

(l) 3rd May 2021.

Figure C3. Boxplots of the bias calculated as the Mean SWE generated by the proposed approach minus the ASO product value for each different elevation, slope and aspect belts. The results are represented proposed SWE dataset (in orange) is evaluated against ASO (in blue) for the 12 analyzed dates over the three hydrological seasons (2018-2021) for the South Fork catchment SFSJR (cont.).

Table C1. Results of the intercomparison between the proposed SWE and the WUS-SR dataset versus ASO for the SFSJR. Bias, RMSE, and correlation are calculated pixel-wise. To this purpose, the proposed and ASO SWE maps were aggregated at a resolution of 500 m.

Date	BIAS [mm]		RMSE [mm]		Correlation [-]	
	<u>proposed</u>	<u>WUS-SR</u>	<u>proposed</u>	<u>WUS-SR</u>	<u>proposed</u>	<u>WUS-SR</u>
<u>2019/03/17</u>	<u>-121</u>	<u>36</u>	<u>242</u>	<u>292</u>	<u>0.80</u>	<u>0.66</u>
<u>2019/05/02</u>	<u>-61</u>	<u>-4</u>	<u>208</u>	<u>307</u>	<u>0.90</u>	<u>0.77</u>
<u>2019/06/09</u>	<u>-25</u>	<u>-32</u>	<u>182</u>	<u>302</u>	<u>0.93</u>	<u>0.79</u>
<u>2019/07/04</u>	<u>-49</u>	<u>-14</u>	<u>129</u>	<u>201</u>	<u>0.90</u>	<u>0.71</u>
<u>2019/07/14</u>	<u>-51</u>	<u>-20</u>	<u>125</u>	<u>163</u>	<u>0.84</u>	<u>0.65</u>
<u>2020/04/15</u>	<u>-73</u>	<u>-26</u>	<u>159</u>	<u>169</u>	<u>0.80</u>	<u>0.78</u>
<u>2020/05/05</u>	<u>-59</u>	<u>5</u>	<u>151</u>	<u>154</u>	<u>0.82</u>	<u>0.80</u>
<u>2020/05/23</u>	<u>-95</u>	<u>-27</u>	<u>179</u>	<u>150</u>	<u>0.79</u>	<u>0.78</u>
<u>2020/06/08</u>	<u>-25</u>	<u>3</u>	<u>96</u>	<u>100</u>	<u>0.72</u>	<u>0.70</u>
<u>2021/02/26</u>	<u>5</u>	<u>96</u>	<u>92</u>	<u>157</u>	<u>0.75</u>	<u>0.65</u>
<u>2021/03/31</u>	<u>74</u>	<u>119</u>	<u>124</u>	<u>202</u>	<u>0.85</u>	<u>0.72</u>
<u>2021/05/03</u>	<u>65</u>	<u>54</u>	<u>121</u>	<u>121</u>	<u>0.89</u>	<u>0.66</u>

925 *Competing interests.* The authors declare that they have no conflict of interest.

Acknowledgements. This work was supported by the joint project Swiss National Science Foundation (SNF) ~~project-~~ Autonomous Province of Bolzano (Italy) "Snowtinel: Sentinel-1 SAR assisted catchment hydrology: toward an improved snow-melt dynamics for alpine regions" Contract No. 200021L205190.

We also would like to thank the NASA Airborne Snow Observatory (ASO) for providing free-of-charge data.

930 **References**

- Anderton, S., White, S., and Alvera, B.: Micro-scale spatial variability and the timing of snow melt runoff in a high mountain catchment, *Journal of Hydrology*, 268, 158–176, 2002.
- Archer, D. and Stewart, D.: The Installation and Use of a Snow Pillow to Monitor Snow Water Equivalent, Water and environmental management: journal of the Institution of Water and Environmental Management, 9, 221–230, <https://doi.org/10.1111/j.1747-6593.1995.tb00934.x>, 1995.
- 935 Arsenault, K. R. and Houser, P. R.: Generating observation-based snow depletion curves for use in snow cover data assimilation, *Geosciences*, 8, 484, 2018.
- Baghdadi, N., Gauthier, Y., and Bernier, M.: Capability of multitemporal ERS-1 SAR data for wet-snow mapping, *Remote sensing of environment*, 60, 174–186, 1997.
- 940 Bair, E. H., Rittger, K., Davis, R. E., Painter, T. H., and Dozier, J.: Validating reconstruction of snow water equivalent in California’s Sierra Nevada using measurements from the NASA Airborne Snow Observatory, *Water Resources Research*, 52, 8437–8460, <https://doi.org/https://doi.org/10.1002/2016WR018704>, 2016.
- Balk, B. and Elder, K.: Combining binary decision tree and geostatistical methods to estimate snow distribution in a mountain watershed, *Water Resources Research*, 36, 13–26, 2000.
- 945 Barella, R., Marin, C., Gianinetto, M., and Notarnicola, C.: A novel approach to high resolution snow cover fraction retrieval in mountainous regions, in: *IGARSS 2022-2022 IEEE International Geoscience and Remote Sensing Symposium*, pp. 3856–3859, IEEE, 2022.
- Beniston, M., Farinotti, D., Stoffel, M., Andreassen, L. M., Coppola, E., Eckert, N., Fantini, A., Giacona, F., Hauck, C., Huss, M., et al.: The European mountain cryosphere: a review of its current state, trends, and future challenges, *Cryosphere*, 12, 759–794, 2018.
- Cline, D. W., Bales, R. C., and Dozier, J.: Estimating the spatial distribution of snow in mountain basins using remote sensing and energy balance modeling, *Water Resources Research*, 34, 1275–1285, 1998.
- 950 Deschamps-Berger, C., Gascoin, S., Berthier, E., Deems, J., Gutmann, E., Dehecq, A., Shean, D., and Dumont, M.: Snow depth mapping from stereo satellite imagery in mountainous terrain: evaluation using airborne laser-scanning data, *The Cryosphere*, 14, 2925–2940, <https://doi.org/10.5194/tc-14-2925-2020>, 2020.
- DeWalle, D. and Rango, A.: Modelling snowmelt runoff, *Principles of Snow Hydrology*. Cambridge University Press, New York, USA, pp. 266–305, 2008.
- 955 Dietz, A. J., Kuenzer, C., Gessner, U., and Dech, S.: Remote sensing of snow—a review of available methods, *International Journal of Remote Sensing*, 33, 4094–4134, 2012.
- Dong, C.: Remote sensing, hydrological modeling and in situ observations in snow cover research: A review, *Journal of Hydrology*, 561, 573–583, 2018.
- 960 Durand, M., Molotch, N. P., and Margulis, S. A.: Merging complementary remote sensing datasets in the context of snow water equivalent reconstruction, *Remote Sensing of Environment*, 112, 1212–1225, 2008.
- Endrizzi, S., Gruber, S., Dall’Amico, M., and Rigon, R.: GEOtop 2.0: simulating the combined energy and water balance at and below the land surface accounting for soil freezing, snow cover and terrain effects, *Geoscientific Model Development*, 7, 2831–2857, 2014.
- Engel, M., Notarnicola, C., Endrizzi, S., and Bertoldi, G.: Snow model sensitivity analysis to understand spatial and temporal snow dynamics in a high-elevation catchment, *Hydrological processes*, 31, 4151–4168, 2017.
- 965

- Fang, Y., Liu, Y., and Margulis, S.: Western United States UCLA Daily Snow Reanalysis, Version 1.[Indicate subset used], Boulder, Colorado USA. NASA National Snow and Ice Data Center Distributed Active Archive Center. doi: <https://doi.org/10.5067/PP7T2GBI52I2>. [Date Accessed], 760, 2022.
- 970 Fehlmann, M., Gascón, E., Rohrer, M., Schwarb, M., and Stoffel, M.: Estimating the snowfall limit in alpine and pre-alpine valleys: A local evaluation of operational approaches, *Atmospheric Research*, 204, 136–148, 2018.
- Guneriussen, T., Hogda, K. A., Johnsen, H., and Lauknes, I.: InSAR for estimation of changes in snow water equivalent of dry snow, *IEEE Transactions on Geoscience and Remote Sensing*, 39, 2101–2108, 2001.
- Günther, D., Marke, T., Essery, R., and Strasser, U.: Uncertainties in snowpack simulations—Assessing the impact of model structure, parameter choice, and forcing data error on point-scale energy balance snow model performance, *Water Resources Research*, 55, 2779–975 2800, 2019.
- Hall, D. and Riggs, G.: MODIS/Terra Snow Cover Daily L3 Global 500 m SIN Grid,[2000–2021], Version 61, 2021.
- Helfricht, K., Hartl, L., Koch, R., Marty, C., and Olefs, M.: Obtaining sub-daily new snow density from automated measurements in high mountain regions, *Hydrology and Earth System Sciences*, 22, 2655–2668, 2018.
- Hock, R.: Temperature index melt modelling in mountain areas, *Journal of Hydrology*, 282, 104–115, 980 [https://doi.org/https://doi.org/10.1016/S0022-1694\(03\)00257-9](https://doi.org/https://doi.org/10.1016/S0022-1694(03)00257-9), *mountain Hydrology and Water Resources*, 2003.
- Immerzeel, W. W., Lutz, A., Andrade, M., Bahl, A., Biemans, H., Bolch, T., Hyde, S., Brumby, S., Davies, B., Elmore, A., et al.: Importance and vulnerability of the world’s water towers, *Nature*, 577, 364–369, 2020.
- Ismail, M. F., Bogacki, W., Disse, M., Schäfer, M., and Kirschbauer, L.: Estimating degree-day factors of snow based on energy flux components, *The Cryosphere*, 17, 211–231, 2023.
- 985 Jost, G., Weiler, M., Gluns, D. R., and Alila, Y.: The influence of forest and topography on snow accumulation and melt at the watershed-scale, *Journal of Hydrology*, 347, 101–115, 2007.
- Lehning, M., Völksch, I., Gustafsson, D., Nguyen, T. A., Stähli, M., and Zappa, M.: ALPINE3D: a detailed model of mountain surface processes and its application to snow hydrology, *Hydrological Processes: An International Journal*, 20, 2111–2128, 2006.
- Leinss, S., Wiesmann, A., Lemmetyinen, J., and Hajnsek, I.: Snow water equivalent of dry snow measured by differential interferometry, 990 *IEEE Journal of Selected Topics in Applied Earth Observations and Remote Sensing*, 8, 3773–3790, 2015.
- Li, D., Lettenmaier, D. P., Margulis, S. A., and Andreadis, K.: The value of accurate high-resolution and spatially continuous snow information to streamflow forecasts, *Journal of Hydrometeorology*, 20, 731–749, 2019.
- Lievens, H., Brangers, I., Marshall, H.-P., Jonas, T., Olefs, M., and De Lannoy, G.: Sentinel-1 snow depth retrieval at sub-kilometer resolution over the European Alps, *The Cryosphere*, 16, 159–177, 2022.
- 995 Luce, C. H., Tarboton, D. G., and Cooley, K. R.: The influence of the spatial distribution of snow on basin-averaged snowmelt, *Hydrological Processes*, 12, 1671–1683, 1998.
- Mair, E., Bertoldi, G., Leitinger, G., Della Chiesa, S., Niedrist, G., and Tappeiner, U.: ESOLIP—estimate of solid and liquid precipitation at sub-daily time resolution by combining snow height and rain gauge measurements, *Hydrology and Earth System Sciences Discussions*, 10, 8683–8714, 2013.
- 1000 Marin, C., Bertoldi, G., Premier, V., Callegari, M., Brida, C., Hürkamp, K., Tschiersch, J., Zebisch, M., and Notarnicola, C.: Use of Sentinel-1 radar observations to evaluate snowmelt dynamics in alpine regions, *The Cryosphere*, 14, 935–956, 2020.
- Martinec, J. and Rango, A.: Areal Distribution of Snow Water Equivalent Evaluated by Snow Cover Monitoring, *Water Resources Research*, 17, 1480–1488, <https://doi.org/10.1029/WR017i005p01480>, 1981.

- Meløysund, V., Leira, B., Høiset, K. V., and Lisø, K. R.: Predicting snow density using meteorological data, *Meteorological Applications: A journal of forecasting, practical applications, training techniques and modelling*, 14, 413–423, 2007.
- 1005 Mendoza, P. A., Musselman, K. N., Revuelto, J., Deems, J. S., López-Moreno, J. I., and McPhee, J.: Interannual and seasonal variability of snow depth scaling behavior in a subalpine catchment, *Water Resources Research*, 56, e2020WR027343, 2020.
- Molotch, N. P. and Bales, R. C.: Scaling snow observations from the point to the grid element: Implications for observation network design, *Water Resources Research*, 41, 2005.
- 1010 Molotch, N. P. and Bales, R. C.: Comparison of ground-based and airborne snow surface albedo parameterizations in an alpine watershed: Impact on snowpack mass balance, *Water Resources Research*, 42, 2006.
- Molotch, N. P. and Margulis, S. A.: Estimating the distribution of snow water equivalent using remotely sensed snow cover data and a spatially distributed snowmelt model: A multi-resolution, multi-sensor comparison, *Advances in water resources*, 31, 1503–1514, 2008.
- Molotch, N. P., Painter, T. H., Bales, R. C., and Dozier, J.: Incorporating remotely-sensed snow albedo into a spatially-distributed snowmelt model, *Geophysical Research Letters*, 31, 2004.
- 1015 Mott, R., Vionnet, V., and Grünewald, T.: The seasonal snow cover dynamics: review on wind-driven coupling processes, *Frontiers in Earth Science*, 6, 197, 2018.
- Murphy, B., Müller, S., and Yurchak, R.: *GeoStat-Framework/PyKrige: v1. 5.0*, Version v1, 5, 2020.
- Musselman, K. N., Clark, M. P., Liu, C., Ikeda, K., and Rasmussen, R.: Slower snowmelt in a warmer world, *Nature Climate Change*, 7, 214–219, 2017.
- 1020 Nagler, T. and Rott, H.: Retrieval of wet snow by means of multitemporal SAR data, *IEEE Transactions on Geoscience and Remote Sensing*, 38, 754–765, 2000.
- Painter, T. H., Berisford, D. F., Boardman, J. W., Bormann, K. J., Deems, J. S., Gehrke, F., Hedrick, A., Joyce, M., Laidlaw, R., Marks, D., et al.: The Airborne Snow Observatory: Fusion of scanning lidar, imaging spectrometer, and physically-based modeling for mapping snow water equivalent and snow albedo, *Remote Sensing of Environment*, 184, 139–152, 2016.
- 1025 Parajka, J. and Blöschl, G.: Validation of MODIS snow cover images over Austria, 2006.
- Pimentel, R., Herrero, J., Zeng, Y., Su, Z., and Polo, M. J.: Study of snow dynamics at subgrid scale in semiarid environments combining terrestrial photography and data assimilation techniques, *Journal of hydrometeorology*, 16, 563–578, 2015.
- Pimentel, R., Herrero, J., and Polo, M. J.: Subgrid parameterization of snow distribution at a Mediterranean site using terrestrial photography, *Hydrology and Earth System Sciences*, 21, 805–820, 2017.
- 1030 Prein, A. F. and Gobiet, A.: Impacts of uncertainties in European gridded precipitation observations on regional climate analysis, *International Journal of Climatology*, 37, 305–327, 2017.
- Premier, V., Marin, C., Steger, S., Notarnicola, C., and Bruzzone, L.: A Novel Approach Based on a Hierarchical Multiresolution Analysis of Optical Time Series to Reconstruct the Daily High-Resolution Snow Cover Area, *IEEE Journal of Selected Topics in Applied Earth Observations and Remote Sensing*, 14, 9223–9240, 2021.
- 1035 Pulliainen, J., Luojus, K., Derksen, C., Mudryk, L., Lemmetyinen, J., Salminen, M., Ikonen, J., Takala, M., Cohen, J., Smolander, T., et al.: Patterns and trends of Northern Hemisphere snow mass from 1980 to 2018, *Nature*, 581, 294–298, 2020.
- Rees, W. G.: *Remote sensing of snow and ice*, CRC press, 2005.
- Revuelto, J., Alonso-González, E., Gascoin, S., Rodríguez-López, G., and López-Moreno, J. I.: Spatial Downscaling of MODIS Snow Cover Observations Using Sentinel-2 Snow Products, *Remote Sensing*, 13, 4513, 2021.
- 1040

- Rittger, K., Bair, E. H., Kahl, A., and Dozier, J.: Spatial estimates of snow water equivalent from reconstruction, *Advances in Water Resources*, 94, 345–363, <https://doi.org/https://doi.org/10.1016/j.advwatres.2016.05.015>, 2016.
- Rott, H., Yueh, S. H., Cline, D. W., Duguay, C., Essery, R., Haas, C., Heliere, F., Kern, M., Macelloni, G., Malnes, E., et al.: Cold regions hydrology high-resolution observatory for snow and cold land processes, *Proceedings of the IEEE*, 98, 752–765, 2010.
- 1045 Salomonson, V. V. and Appel, I.: Estimating fractional snow cover from MODIS using the normalized difference snow index, *Remote sensing of environment*, 89, 351–360, 2004.
- Schattan, P., Köhli, M., Schrön, M., Baroni, G., and Oswald, S. E.: Sensing area-average snow water equivalent with cosmic-ray neutrons: The influence of fractional snow cover, *Water Resources Research*, 55, 10796–10812, 2019.
- Shi, J., Dozier, J., and Rott, H.: Snow mapping in alpine regions with synthetic aperture radar, *IEEE Transactions on Geoscience and Remote Sensing*, 32, 152–158, 1994.
- 1050 Shimada, M., Itoh, T., Motooka, T., Watanabe, M., Shiraishi, T., Thapa, R., and Lucas, R.: New global forest/non-forest maps from ALOS PALSAR data (2007–2010), *Remote Sensing of environment*, 155, 13–31, 2014.
- Slater, A., Barrett, A., Clark, M., Lundquist, J., and Raleigh, M.: Uncertainty in seasonal snow reconstruction: Relative impacts of model forcing and image availability, *Advances in Water Resources*, 55, 165–177, <https://doi.org/https://doi.org/10.1016/j.advwatres.2012.07.006>,
- 1055 snow–Atmosphere Interactions and Hydrological Consequences, 2013a.
- Slater, A., Barrett, A., Clark, M., Lundquist, J., and Raleigh, M.: Uncertainty in seasonal snow reconstruction: Relative impacts of model forcing and image availability, *Advances in water resources*, 55, 165–177, 2013b.
- Thorp, J. M. and Scott, B. C.: Preliminary calculations of average storm duration and seasonal precipitation rates for the northeast sector of the United States, *Atmospheric Environment (1967)*, 16, 1763–1774, 1982.
- 1060 Tsang, L., Durand, M., Derksen, C., Barros, A. P., Kang, D.-H., Lievens, H., Marshall, H.-P., Zhu, J., Johnson, J., King, J., et al.: Global Monitoring of Snow Water Equivalent using High Frequency Radar Remote Sensing, *The Cryosphere Discussions*, pp. 1–57, 2021.
- Ulaby, F. T., Moore, R. K., and Fung, A. K.: *Microwave remote sensing: Active and passive. volume 1-microwave remote sensing fundamentals and radiometry*, 1981.
- Vionnet, V., Brun, E., Morin, S., Boone, A., Faroux, S., Le Moigne, P., Martin, E., and Willemet, J.-M.: The detailed snowpack scheme Crocus and its implementation in SURFEX v7. 2, *Geoscientific Model Development*, 5, 773–791, 2012.
- 1065 Viviroli, D., Weingartner, R., and Messerli, B.: Assessing the hydrological significance of the world’s mountains, *Mountain research and Development*, 23, 32–40, 2003.
- Warscher, M., Marke, T., and Strasser, U.: Operational and experimental snow observation systems in the upper Rofental: data from 2017–2020, *Earth System Science Data Discussions*, pp. 1–24, 2021.
- 1070 Yang, K., Musselman, K. N., Rittger, K., Margulis, S. A., Painter, T. H., and Molotch, N. P.: Combining ground-based and remotely sensed snow data in a linear regression model for real-time estimation of snow water equivalent, *Advances in Water Resources*, 160, 104075, 2022.
- Zupanc, A.: Improving cloud detection with machine learning, Accessed: Oct, 10, 2019, 2017.